



Optimized local geometry and electronic structure of MoO₃/CeO₂ catalyst by adding copper cations for boosted nitrogen oxide reduction performance

Hao Liu^a, Chuan Gao^a, Jianjun Chen^{a,*}, Jinxing Mi^a, Shan Yang^b, Deli Chen^a, Wenzhe Si^a, Yue Peng^a, Chuanzhi Sun^b, Junhua Li^{a,*}

^a State Key Joint Laboratory of Environment Simulation and Pollution Control, School of Environment, Tsinghua University, Beijing 100084, PR China

^b College of Chemistry, Chemical Engineering and Materials Science, Shandong Normal University, Jinan 250014, PR China

ARTICLE INFO

Keywords:

NH₃-SCR
MoO₃/CeO₂ catalyst
Cu modification
Electron interaction
Reaction mechanism

ABSTRACT

The construction of highly active centers over the CeO₂-based catalyst for the low-temperature NH₃ selective catalytic reduction of nitrogen oxides (NH₃-SCR) technology in non-power industry is one of the challenges in the application field. Herein, the SCR performance of MoO₃/CeO₂ catalyst has been remarkably enhanced by introducing Cu to induce the generation of active Mo=O structure. Advanced spectroscopy characterizations reveal that the adding of Cu into MoO₃/CeO₂ catalyst could create unsaturated sites on CeO₂ for Mo anchor, and the enhanced electrons transfer from Mo to Cu would cause the formation of a new terminal Mo=O with highly distorted octahedral geometry, which is a new Lewis acid site for coordinated NH₃ production. Meanwhile, the added Cu creates the adsorbed site for gaseous NO and the formed Mo-O-Cu pair center facilitates the transformation of ionic NO₂⁻ generated from NO adsorption to NO₂, which is conducive to the fast SCR reaction process.

1. Introduction

Urban ozone and particulate matter are still severe air pollution issues that human beings are facing. The nitrogen oxides (NO_x, x = 1 and 2) emitted from fossil fuel combustion are important factors to cause these pollution problems [1,2]. Up to now, ammonia selective catalytic reduction (NH₃-SCR) approach is recognized as an effectively method to purify NO_x emissions, in which catalyst is the core of this technology [3]. Relevant research manifested that V₂O₅-based [4,5], MnO_x-based [6,7], Fe₂O₃-based [8,9], and CeO₂-based [10,11] catalysts are considered as forceful candidates for NH₃-SCR. Especially, V₂O₅-WO₃(MoO₃)/TiO₂ catalyst has already been put into commercial adhibition, but the poor N₂ selectivity and the volatilization of toxic active component vanadium at high temperature inhibited its further development [8,12]. Hence, the development of free and non-toxic V₂O₅-based metal oxide catalysts with wide operating temperature window, high N₂ selectivity, and durability to H₂O/SO₂ is a hotspot in deNO_x field [3].

By virtue of special electronic configuration, CeO₂ exhibits excellent redox performance due to good Ce^{3+/4+} switching ability and attracted more attention in the field of environmental catalysis [11,13]. On the one hand, researchers are committed to explore the role of cerium as an

assistant. For instance, Gevers et al. [7] investigated the CeO₂-MnO_x-TiO₂ ternary mixed oxide catalyst and found that Ce, as a structural promoter, declined the average valence state of the active species Mn, as well as inhibited the formation of N₂O through the dilution effect on the active species of MnO_x. Chen et al. [8] synthesized single-atom Ce modified Fe₂O₃ catalyst by citric acid method, and the generation of Ce-O-Fe link can boost the oxidation of NO to NO₂, thus greatly enhancing the NO_x removal efficiency. On the other hand, CeO₂ also exhibits a certain catalytic ability for NH₃-SCR reaction, while some additives were usually introduced into the pure CeO₂ to acquire a better performance. Tan et al. [14] designed a novel CeO₂-SiO₂ mixed oxide with rich Ce-O-Si sites and surface hydroxyl groups, of which the "mechanism-enhanced process" induced by its special surface structure made this catalyst exhibit excellent SCR activity with high SO₂ tolerance. It can be seen from the above examples that it is a frequently-used strategy for improving the SCR performance of CeO₂-based catalysts via regulating the surface acidity and redox properties.

As a classic Ce-based NH₃-SCR catalyst system, MoO₃-CeO₂ composite oxides have competitive NO_x conversion, N₂ selectivity, and good SO₂ + H₂O tolerance in the range of 250–400 °C, which have received more and more attention from investigators. Therefore, MoO₃-CeO₂

* Corresponding authors.

E-mail addresses: chenjianjun@tsinghua.edu.cn (J. Chen), lijunhua@tsinghua.edu.cn (J. Li).

<https://doi.org/10.1016/j.apcatb.2023.122742>

Received 30 January 2023; Received in revised form 29 March 2023; Accepted 5 April 2023

Available online 6 April 2023

0926-3373/© 2023 Elsevier B.V. All rights reserved.

catalyst has great practical application potential in SCR technology at medium-high temperature stages [15]. Such performance is not possessed by other Ce-based catalysts systems. For example, although $\text{MnO}_x\text{-CeO}_2$ catalysts have excellent low-temperature NO_x conversion, their N_2 selectivity is poor and they are prone to deactivation due to SO_2 and HCl erosion [16]. In our previous research [17], it was found that the $\text{MoO}_3\text{-CeO}_2$ catalyst involved a dual cycle process in the $\text{NH}_3\text{-SCR}$ mechanism, as shown in Scheme 1. One is the acid sites cycle arising from the Brønsted acid site provided by the MoO_3 species, and the other is the redox cycle induced by the excellent oxygen storage and reduction properties of CeO_2 . This means that the synergistic effect between Mo and Ce species in $\text{MoO}_3\text{-CeO}_2$ composite oxides makes it an interesting catalytic system for $\text{NH}_3\text{-SCR}$. Nevertheless, it is worth noting that the SCR activity of $\text{MoO}_3\text{-CeO}_2$ catalyst system has not yet achieved satisfactory results. The first reason is the insufficient quantity of Lewis acid sites. This is of great importance because Lewis acid presents higher intrinsic reactivity than Brønsted acid at low temperatures ($\leq 200^\circ\text{C}$) [18]. Moreover, the redox ability of $\text{MoO}_3/\text{CeO}_2$ catalysts is weak at low temperatures, which has been confirmed by $\text{H}_2\text{-TPR}$ experiments [15, 17]. Another important consequence is that the catalyst has insufficient activation capacity for NO , which hinders the "fast-SCR" pathway during SCR course. A simple and effective method to achieve the improved SCR performance is through the geometric/electronic structure regulation of the active site by adding secondary species. $\text{Cu}^{\delta+}$ ($\delta = 0, 1, 2$) cations have a special orbital electronic structure, and as modifiers, they can effectively improve the geometric and electronic structure of the parent catalyst [19]. Relevant research also verified that the SCR activity can be observably boosted by introducing a low-content of $\text{Cu}^{\delta+}$ into the $\text{TiO}_2/\text{CeO}_2$ and $\text{Nb}_2\text{O}_5/\text{CeO}_2$ catalyst [12,20].

In this work, the $\text{MoO}_3/\text{CuO}_x/\text{CeO}_2$ catalyst optimized by step impregnation exhibited the best $\text{NH}_3\text{-SCR}$ activity and $\text{H}_2\text{O}/\text{SO}_2$ tolerance than that of $\text{MoO}_3/\text{CeO}_2$ and $\text{CuO}_x/\text{MoO}_3/\text{CeO}_2$ catalysts. Following the concept of "performance test \rightarrow geometric/electronic structure characterization \rightarrow structure-activity relationship", this study systematically investigated the influence of $\text{Cu}^{\delta+}$ species introduction method on the intrinsic physico-chemical properties, catalytic activity and reaction mechanism of $\text{MoO}_3/\text{CeO}_2$ catalyst, so as to establish the structure-activity relationship of $\text{MoO}_3/\text{CuO}_x/\text{CeO}_2$ catalyst in $\text{NH}_3\text{-SCR}$ course. Thereinto, the surface structure of the as-synthesized catalysts was unambiguously clarified by a series of advanced characterizations techniques. The electronic interaction among Cu, Mo and Ce was precisely analyzed by X-ray photoelectron spectroscopy (XPS) and X-ray absorption near edge structure (XANES), as well as density functional theory (DFT), and was further supplemented by hydrogen temperature programmed reduction ($\text{H}_2\text{-TPR}$). During the reaction, the adsorption behavior of reaction molecules on the catalyst surface and the dynamic evolution of the surface structure were probed through *in situ* diffuse reflectance Fourier transform infrared spectroscopy (DRIFTS) combined

with *in situ* Raman.

2. Experimental

2.1. Catalyst preparation

Bare CeO_2 support was synthesized by hydrothermal method. Typically, dissolve 2 mmol of cerous chloride (CeCl_3 , Shanghai Macklin Biochemical Co.,Ltd., 99.99%) and 9.6 g of sodium hydroxide (NaOH , Shanghai Macklin Biochemical Co.,Ltd., 97%) into a total of 40 mL of deionized water respectively, and mix and stir for 1 h after completely dissolving to room temperature. Move it into 50 mL Teflon-lined stainless steel and heat it for 18 h at 140°C . Centrifuge the product and wash it to neutral (10 times with deionized water and 1 time with absolute ethanol). Dry for more than 12 h at 110°C in the oven. Calcine at 550°C for 4 h in muffle furnace, with 1°C min^{-1} heating rate. Bare CeO_2 support is thus obtained.

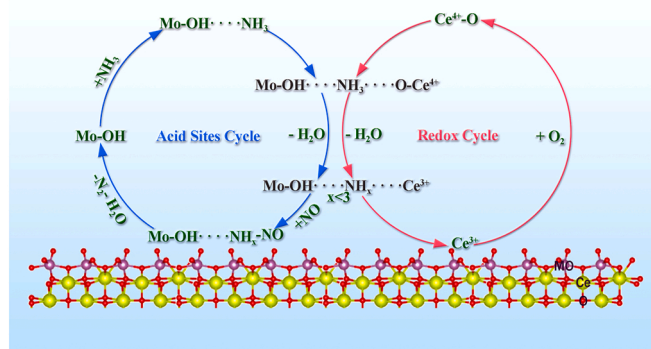
The second step, ammonium molybdate tetrahydrate ($\text{H}_24\text{Mo}_7\text{N}_6\text{O}_{24}\cdot 4\text{H}_2\text{O}$, 99%, Macklin) and copper nitrate hemi-pentahydrate ($\text{Cu}(\text{NO}_3)_2\cdot 2.5\text{H}_2\text{O}$, 98%, Macklin) were used as precursors respectively, and the traditional wet-impregnation method was used to load MoO_3 and CuO_x . Specifically, dissolve the required amount of $\text{H}_24\text{Mo}_7\text{N}_6\text{O}_{24}\cdot 4\text{H}_2\text{O}$ and $\text{Cu}(\text{NO}_3)_2\cdot 2.5\text{H}_2\text{O}$ in 100 mL deionized water respectively, and then add 5 g CeO_2 to the above two solutions respectively, and continue stirring for 2 h. Then evaporate to dryness (80°C , water bath). The resulting solids were placed in an oven at 110°C for 12 h. Finally, calcine in a muffle furnace at 500°C for 4 h, and the heating rate is 1°C min^{-1} . So as to obtain $\text{MoO}_3/\text{CeO}_2$ and $\text{CuO}_x/\text{CeO}_2$ samples.

The third step, continue to dissolve the required amount of $\text{H}_24\text{Mo}_7\text{N}_6\text{O}_{24}\cdot 4\text{H}_2\text{O}$ and $\text{Cu}(\text{NO}_3)_2\cdot 2.5\text{H}_2\text{O}$ in 60 mL of deionized water, and then add 3.03 g of $\text{CuO}_x/\text{CeO}_2$ and 3.12 g of $\text{MoO}_3/\text{CeO}_2$ respectively to the above solution, and continue stirring for 2 h. Then repeat step 2. Thus, $\text{MoO}_3/\text{CuO}_x/\text{CeO}_2$ and $\text{CuO}_x/\text{MoO}_3/\text{CeO}_2$ catalysts were obtained. The loading amounts of CuO_x and MoO_3 are 1 wt% and 4 wt%, respectively (for the mass of CeO_2). The as-synthesized $\text{CuO}_x/\text{CeO}_2$, $\text{MoO}_3/\text{CeO}_2$, $\text{CuO}_x/\text{MoO}_3/\text{CeO}_2$ and $\text{MoO}_3/\text{CuO}_x/\text{CeO}_2$ samples were labeled as Cu/Ce, Mo/Ce, Cu/Mo/Ce and Mo/Cu/Ce, respectively.

2.2. Catalyst characterization and DFT calculation

X-ray powder diffraction patterns (XRD) were performed by the D8/Advance X-ray diffractometer from BRUKER, Germany, equipped with $\text{Cu K}\alpha$ X-ray source, $\lambda = 1.5408 \text{ \AA}$, 40 kV and 20 mA, and the scanning rate is 2° min^{-1} in the range of $10^\circ\text{--}90^\circ$. Raman is carried on Horiba LaRAM HR Evolution (Horiba Jobin Yvon) with 532 nm of the laser wavelength. The tests of inductively coupled plasma-optical emission spectroscopy (ICP-OES) were performed on iCAP 7000 spectrometer from Thermo Fisher Scientific. Low-temperature N_2 adsorption-desorption technology was carried out on Micrometrics ASAP-2460 to acquire the specific surface area of the sample. Scanning electron microscope (SEM) images were obtained using S-4800 Hitachi at 5 kV acceleration voltage. High-angle annular dark field (HAADF) images were obtained on FEI Titan 80-300 field emission spherical aberration corrected scanning transmission electron microscope (STEM) with the energy resolution $\leq 0.7 \text{ eV}$.

The measurements of X-ray photoelectron spectroscopy (XPS) were performed on ESCALAB 250XI photoelectron spectrometer (Thermo Scientific, USA), $\text{Al K}\alpha$ X-ray, 14 kV working voltage, and the electron binding energy of the elements is corrected by C 1s (284.8 eV). The X-ray absorption spectra (XAS) including X-ray absorption near-edge structure (XANES) and extended X-ray absorption fine structure (EXAFS) of the samples at Cu K-edge and Mo K-edge were collected at the Singapore Synchrotron Light Source (SSLS) center, where a pair of channel-cut Si (111) crystals was used in the monochromator. The Cu/Mo K-edge XANES data were recorded in a transmission mode. The storage ring was working at the energy of 2.5 GeV with an average



Scheme 1. A schematic diagram for the $\text{NH}_3\text{-SCR}$ pathway over the $\text{MoO}_3/\text{CeO}_2$ catalyst.

electron current of below 200 mA. The acquired EXAFS data were extracted and processed according to the standard procedures using the ATHENA module implemented in the FEFFIT software packages.

Hydrogen temperature-programmed reduction (H_2 -TPR) is performed on the Chemisorb 2920 chemical adsorption analyzer (Micromeritics, USA). NH_3 and $NO+O_2$ temperature programmed desorption (TPD) tests were employed on GASMET DX-4000. The sample mass was 100 mg. Before the test, all samples were treated at 400 °C in high-purity N_2 atmosphere for one hour. *In situ* diffused reflectance infrared Fourier transform spectroscopy (*in situ* DRIFTS), and *in situ* Raman were performed on NICOLET 6700 FT-IR spectrometer (Thermo Fisher, USA) with a Harrick IR cell, and Horiba LaRAM HR Evolution (Horiba Jobin Yvon), respectively. The samples were treated in helium environment at 400 °C for one hour before the test. During the test, $[NO_x] = [NH_3] = 500$ ppm, $[O_2] = 5$ vol%, $[SO_2] = 500$ ppm. The combination of thermogravimetric (TG, STA 8000, PerkinElmer) and FTIR spectrometer (Frontier, PerkinElmer) was conducted to investigate the decomposition/release temperature and composition of the surface sulfate species on the $SO_2 + H_2O$ durability-tested catalyst.

All the spin-polarized density functional theory (DFT) calculations were conducted by using the Vienna ab initio simulation package (VASP). To accurately treat the highly localized Ce 4 f-orbitals, we performed spin-polarized DFT+*U* calculations with *U* = 5.0 eV applied to the Ce 4 f state [21,22]. The projector-augmented wave (PAW) method was utilized to describe the core–valence interaction with an energy cutoff of 400 eV. The generalized gradient approximation (GGA) with the Perdew–Burke–Ernzerhof (PBE) exchange–correlation functional was used. The Gaussian smearing method was employed to set the partial occupancies for each orbital with a smearing width of 0.05 eV. The Brillouin zone was sampled at the $2 \times 3 \times 1$ k-point mesh. The convergence criteria set for energy was 10^{-6} eV. Optimized structures were obtained by minimizing the forces on each ion until they were below 0.02 eV/Å.

2.3. Catalytic performance

The catalytic performance of NO_x removal was evaluated on GASMET DX-4000, a FTIR online gas analyzer. Place 100 mg of catalyst in a fixed-bed quartz reactor. The catalyst was used in simulated flue gas ($[NO_x] = [NH_3] = 500$ ppm ($[NO_x] = [NO] + [NO_2]$), $[O_2] = 5$ vol%, $[SO_2] = 100$ ppm (when used), $[H_2O] = 5$ vol% (when used), and N_2 as balance gas) with a gas hourly space velocity (GHSV) of 60,000 mL $g^{-1} h^{-1}$. Before activity evaluation, the catalyst was treated for 1 h under the conditions of 300 °C and 100 mL min^{-1} high-purity N_2 gas flow. The NO_x conversion, and N_2 selectivity is calculated by the following equation:

$$NO_x \text{ conversion}(\%) = \frac{[NO_x]_{in} - [NO_x]_{out}}{[NO_x]_{in}} \times 100\% \quad (2-1)$$

$$N_2 \text{ selectivity}(\%) = \frac{[NO_x]_{in} - [NO_x]_{out} + [NH_3]_{in} - [NH_3]_{out} - 2[N_2O]_{out}}{[NO_x]_{in} - [NO_x]_{out} + [NH_3]_{in} - [NH_3]_{out}} \times 100\% \quad (2-2)$$

The reaction rate (r , mol $g^{-1} s^{-1}$) was calculated through the following equation:

$$r = -\frac{V_{NO}}{m_{cat} \cdot M_{NO}} \ln(1-X) \quad (2-3)$$

where, the V_{NO} , m_{cat} , M_{NO} and X are the mass flow of NO inject into the reactor, catalyst weight, NO molecular weight and NO conversion, respectively.

Turnover frequencies (TOF) were estimated through dividing the amount of NO molecules converted per second at low conversion (<20%) by the moles of Mo atoms in the surface of both Mo/Ce and Mo/

Cu/Ce catalysts, and was calculated according to Eqs. (2)–(4):

$$TOF = \frac{r}{N \cdot S_{BET}} \quad (2-4)$$

where, N is surface atomic concentration of Mo atoms ($0.72 \text{ mmol } 100 \text{ m}^{-2}$), S_{BET} is specific surface area ($\text{m}^2 \text{ g}^{-1}$).

3. Results and discussion

3.1. Catalytic performance

Fig. 1(a) and (b) show the NO_x conversion and N_2 selectivity for the CeO_2 , Cu/Ce, Mo/Ce, Cu/Mo/Ce, and Mo/Cu/Ce catalysts as a function of temperature during the NH_3 -SCR. As for pristine CeO_2 , the $deNO_x$ activity below 300 °C is relatively poor and reaches a maximum of ca. 65% at 350 °C with ~80% N_2 selectivity. While, the NO_x conversion gave a remarkably increased value of > 90% above 250 °C after the addition of Mo (Mo/Ce) as along with high N_2 selectivity (>90%) in the whole temperature range. Especially, the low-temperature $deNO_x$ activity is further enhanced over the Cu/Mo/Ce and Mo/Cu/Ce catalysts. Compared with the low NO_x conversion of the Cu/Ce, this enhancement could be possibly ascribed to the tuning effect of Cu on the Mo/Ce system. Notably, a better low-temperature NO_x conversion of Mo/Cu/Ce than that of Cu/Mo/Ce catalyst (also for N_2 selectivity) turns out that the different interaction of Mo and Cu species triggered by the loading order of Cu species, which will be discussed in subsequent sections. From the statistical results of the apparent activation energy (Fig. 1(c)), compared to Mo/Ce, the activation energy observably declined after copper species introducing, as well as the activation energy of Mo/Cu/Ce was 6.6 kJ/mol lower than that of Cu/Mo/Ce. This further indicates that the tuning effect induced by diverse CuO_x introduction methods can dramatically influence the intrinsic reaction activity of Mo/Ce catalyst. Fig. 1(d) exhibits the stability test of the Mo/Ce, Cu/Mo/Ce, and Mo/Cu/Ce in the presence of SO_2 and H_2O at 250 °C. In order to scientifically contrast of the SO_2 or/and H_2O durability of the three catalysts, the GHSV was increased to 90,000 mL $g^{-1} h^{-1}$ during the test, so that the three catalysts had approximately the same initial NO_x conversion ($81\% \pm 3\%$). When adding SO_2 in the flue gas, the NO_x conversion of the Cu/Mo/Ce rapidly decreases from ca. 79% to ca. 53%, while the falling range of NO_x conversion over the Mo/Ce and Mo/Cu/Ce is only 19% (from ca. 81% to ca. 62%) and 9% (from ca. 84% to ca. 75%), respectively. This result indicates that Mo sites exhibits better resistance to SO_2 poisoning than that of Cu sites. When SO_2 and water vapor coexist in the flue gas, the NO_x conversion of the three catalysts further decreases. As the reaction time continues for 90 h, the SCR performance remains stable. However, it should be emphasized that during the entire process, the NO_x conversion of Mo/Cu/Ce reduced by ~24%, while the Mo/Ce and Cu/Mo/Ce catalysts declined by ~33% and ~39%, respectively. In conclusion, it is indicated that the suitable introduction of Cu species in the Mo/Ce system could enhance the performance of both the $deNO_x$ activity and the resistance of SO_2 and H_2O .

3.2. Coordination environment of molybdenum and copper

The content of Cu or/and Mo species in Cu/Ce, Mo/Ce, Cu/Mo/Ce and Mo/Cu/Ce samples were tested by ICP-OES, and the results are shown in Table S1. It can be found that the results are substantial agree with the feeding ratio used in the synthesis process. Crystal structure of catalysts was explored by the XRD as displayed in Fig. 2(a). All catalysts exhibit typical CeO_2 phase (PDF: 34–0394) and no new diffraction peaks are detected, indicating that Mo and Cu are uniformly distributed on CeO_2 with amorphous form or tiny microcrystal. Morphology of the catalysts was further investigated by the SEM/ HAADF-STEM and the energy-dispersive X-ray spectroscopy (EDS) to understand the elemental distributions status (Fig. S1). The SEM image shows that CeO_2 exists in

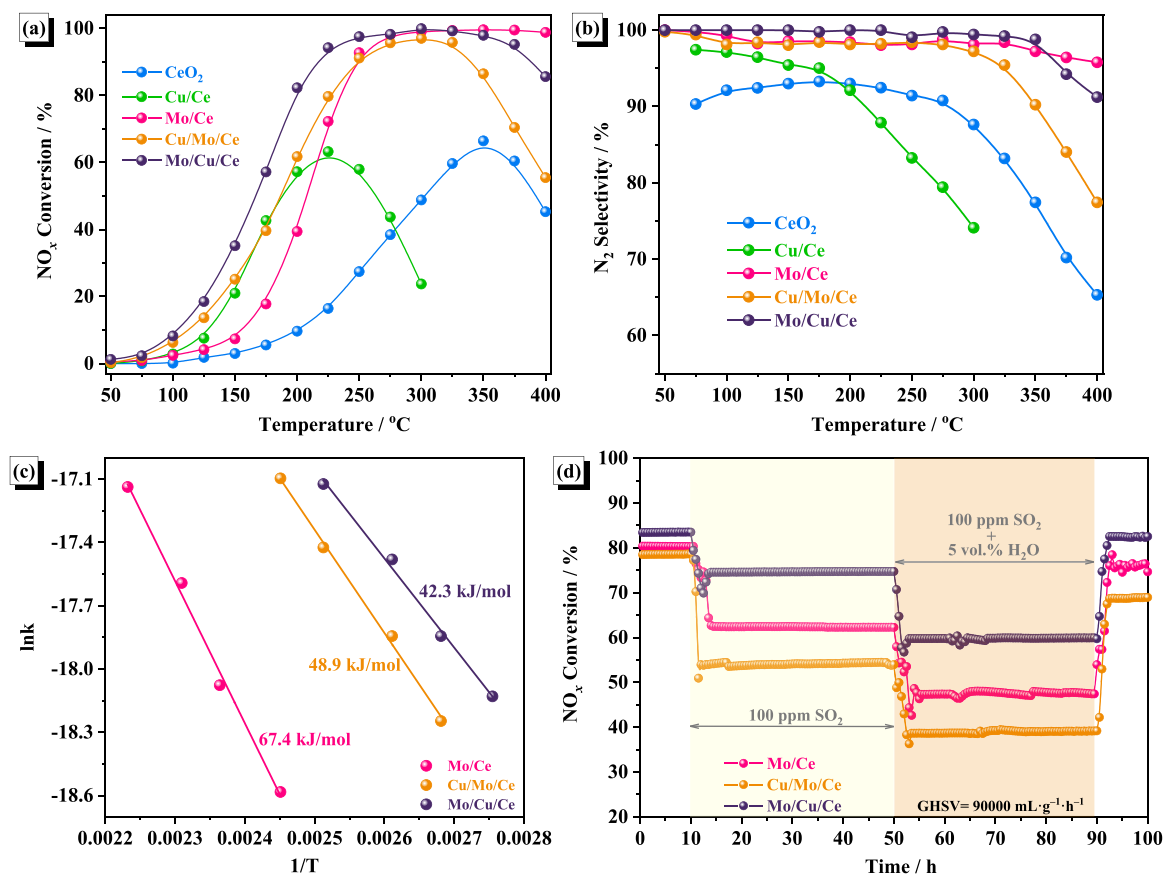


Fig. 1. (a) The NO_x conversion and (b) N₂ selectivity of the CeO₂, Cu/Ce, Mo/Ce, Cu/Mo/Ce, and Mo/Cu/Ce samples. (c) Arrhenius plots for Mo/Ce, Cu/Mo/Ce, and Mo/Cu/Ce catalysts. (d) The durability test of Mo/Ce, Cu/Mo/Ce, and Mo/Cu/Ce catalysts in the presence of SO₂ (100 ppm) or/and H₂O (5 vol%) at 250 °C.

the form of nanorods with abundant surface loose porous structure (Fig. S1(a)). The HAADF-STEM images depict the (111) and (220) lattice planes of CeO₂ with interplanar distance of 0.33 and 0.19 nm, which is consistence with the XRD result. The interplanar distance of the (111) lattice plane is greater than 0.31 nm according to previous works [23, 24], which could be attributed to the doping of Cu cations into CeO₂ lattice. The EDS mapping result demonstrates that Cu and Mo elements are uniformly distributed over the whole CeO₂ nanorods.

The Raman spectra was showed in Fig. 2(b) to investigate the bonding information and the oxidation state of the metal elements in the catalysts. Among, the main peak around 460 cm⁻¹ is attributed to the F_{2g} vibration mode, corresponding to the symmetric vibration of oxygen with adjacent cations in CeO₂ cubic fluorite [13,25]. Meanwhile, the F_{2g} mode peaks of the Cu/Ce, Cu/Mo/Ce, and Mo/Cu/Ce are red-shifted from 463 to 458 cm⁻¹ compared to the CeO₂ and Mo/Ce, which is attributed to the CeO₂ lattice expansion induced by Cu cation doping [24,26]. In addition, the slight peak shift between Cu/Mo/Ce and Mo/Cu/Ce could be caused by the Cu cations were partly bound on the top of the MoO₃ rather than entering the CeO₂ lattice for Cu/Mo/Ce. The weak peaks around 256 and 600 cm⁻¹ are assigned to the longitudinal stretching mode of the Ce-O bond vibration and the defect-induced (D) mode from reduced Ce³⁺ cations [14]. The peak corresponding to the Ce-O bond vibration in the Cu/Ce (244 cm⁻¹) redshifts by 13 cm⁻¹ and the intensity of shoulder at 600 cm⁻¹ increases compared with the CeO₂, while not for the Mo/Ce. This phenomena suggests that Cu could enter into CeO₂ lattice, further resulting in the reduced Ce species to induce the creation of oxygen vacancies [27]. The shift of Ce 3d peaks (Fig. S2 (a)) towards the lower binding energies verifies electron gain of Ce atom after Cu modification. Noted that the peak at 250 cm⁻¹ and the shoulder at 600 cm⁻¹ for the Mo/Cu/Ce are weaker than that of the Cu/Ce, which reveals that Mo species in the Mo/Cu/Ce fill in around oxygen vacancies

and verified by the intensity decline of chemisorbed oxygen on surface oxygen vacancies (O_v) in O 1 s XPS spectra (Fig. S2(b)). Wide bands around 791 and 955 cm⁻¹ are observed on the Mo/Ce, Cu/Mo/Ce, and Mo/Cu/Ce. These bands are assigned to the stretching vibration of Mo-O-Ce and terminal Mo=O originated from the octahedral polymeric Mo species [28,29]. For Cu/Mo/Ce and Mo/Cu/Ce, a new peak around 892 cm⁻¹, related to the stretching vibration of a new type of terminal Mo=O, is found [30]. Considering that the frequency of Mo-O bonds in perfect MoO₄ tetrahedral structure is 858 cm⁻¹, this new terminal Mo=O vibration could derive from a highly distorted structure between octahedron and tetrahedron, indicating that there is intensive interaction between Cu and Mo species through forming Mo-O-Cu bond [29]. The peaks attributed to Mo=O terminals for the Mo/Cu/Ce shift to high wavenumbers by comparison with the Cu/Mo/Ce, which possibly caused by a stronger interaction between Mo species and supports in the Mo/Cu/Ce than that in the Cu/Mo/Ce.

According to the "incorporation model" [31,32], MoO₃, an oxide with weak cohesive energy, can be dispersed on the surface of CeO₂-nanorod in a monolayer. Among them, CeO₂ mainly exposed on the (110) face has a dispersion capacity of 0.74 mmol 100 m⁻². The results of low-temperature N₂ adsorption test showed that the specific surface area of the as-prepared CeO₂ nanorods was 39 m² g⁻¹. In this case, the selected loading amount of MoO₃ is 4 wt%, which is converted to 0.72 mmol 100 m⁻², which is close to the theoretical value. Therefore, MoO₃ completely covers the surface of CeO₂ in the form of monolayer dispersion. Raman spectra also confirmed these results. This provides experimental results support for the construction of the model in this study. Hence, combining Raman, XRD and HAADF-STEM results, we optimized the three models shown in Fig. 2(c-e). On the basis of the classical exposed surface (110) of CeO₂ nanorods, a monolayer of fully loaded MoO₃ was carried out to obtain the MoO₃/CeO₂(110) catalyst

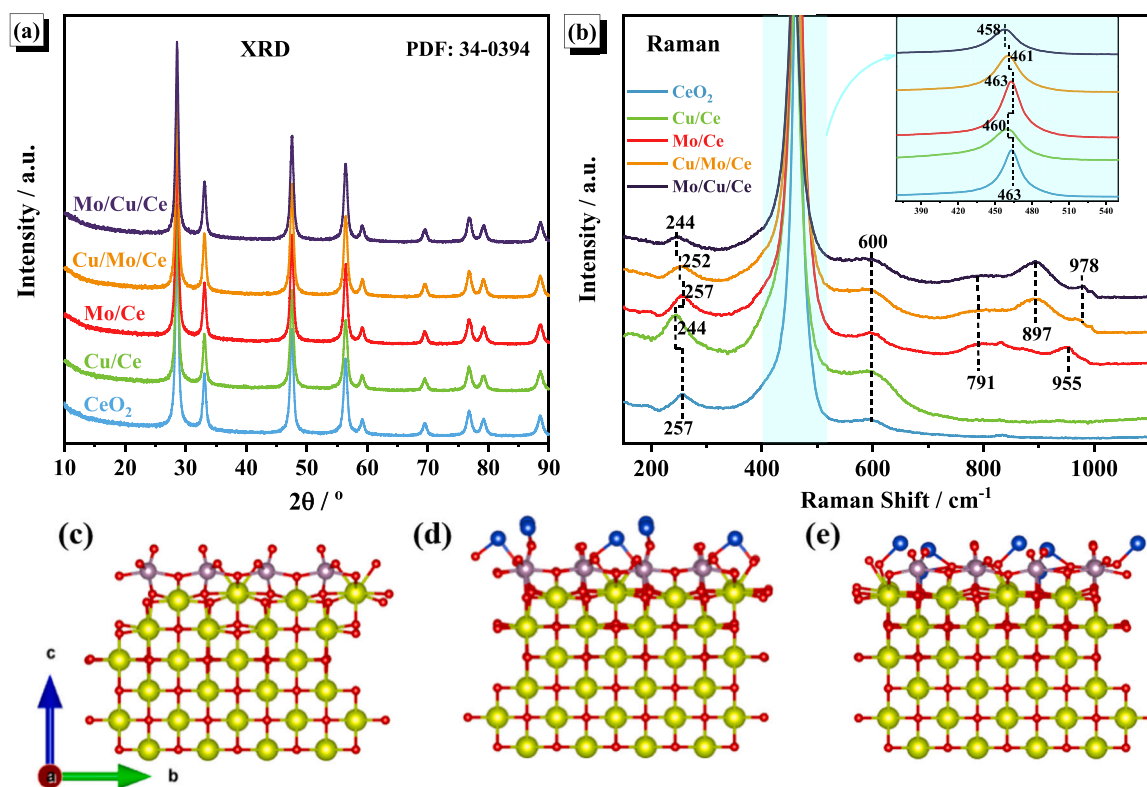


Fig. 2. (a) XRD patterns and (b) Raman spectra of CeO₂, Cu/Ce, Mo/Ce, Cu/Mo/Ce and Mo/Cu/Ce samples. Optimized slab models for (c) MoO₃/CeO₂ (110), (d) CuO_x/MoO₃/CeO₂ (110), and (e) MoO₃/CuO_x/CeO₂ (110) (red: O, yellow: Ce, gray: Mo, blue: Cu).

structure (Fig. 2(c)). After that, CuO_x/MoO₃/CeO₂(110) (Fig. 2(d)) and MoO₃/CuO_x/CeO₂(110) (Fig. 2(e)) were obtained according to the inverse impregnation sequence of Cu species, of which CuO_x clusters were built. Both CuO_x/MoO₃/CeO₂ and MoO₃/CuO_x/CeO₂ catalysts can form Mo-O-Cu bonds, which also has been verified by Raman (Fig. 2(b)). However, the Cu-O-Ce bond differs greatly between Mo/Cu/Ce (Fig. 2(e)) and Cu/Mo/Ce (Fig. 2(d)). This foreboded that on Mo/Cu/Ce and Cu/Mo/Ce catalysts, there are different electron interactions between Cu species and Mo or/ and Ce sites.

The XAFS spectroscopy was carried out to further investigate the electronic structure and local coordination geometry of the catalysts. Fig. 3(a) exhibits normalized Mo K-edge XANES of the Mo/Ce, Cu/Mo/Ce, Mo/Cu/Ce, MoO₃, and Mo foil, where the pre-edge absorption around 20,006 eV corresponds to the forbidden transition from 1 s to 4d

levels in the distortion of Mo-O₆ octahedra, that is the typical feature of orthorhombic α -MoO₃ with Mo⁶⁺ oxidation state [33,34]. For the Mo/Cu/Ce, its pre-edge absorption is higher than that of the Mo/Ce and Cu/Mo/Ce and shifts towards the high energy, suggesting the increased distortion of octahedral Mo oxides geometry as well as the increased oxidation state of Mo [35,36]. According to the results in Raman spectra, the electrons loss of Mo could be ascribed to the electrons transfer from Mo to oxygen vacancies, leading to a stronger interaction among Mo, supports, and further distortion of the Mo octahedral structure. Figs. 3 (b) and S3 show the extended X-ray absorption fine structure (EXAFS) results of all catalysts and reference samples. Three peaks around R = 1.3, 1.9, and 2.3 Å are assigned to the Mo-O, Mo-Mo, and Mo-O-Mo scattering feature, respectively [36]. Two main peaks at 2.5 and 3.1 Å in the Mo foil and MoO₃ references correspond to Mo-Mo and Mo-O

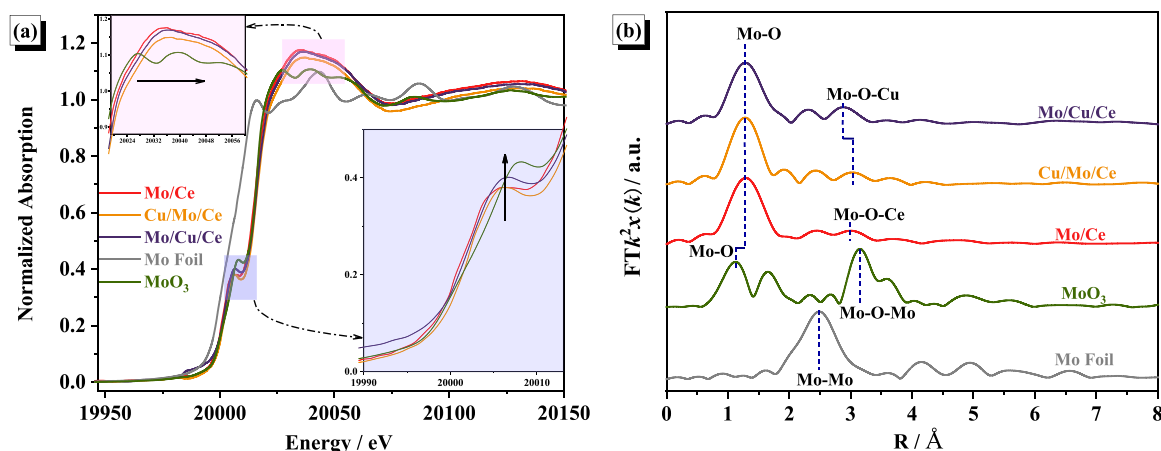


Fig. 3. (a) The normalized Mo K-edge XANES and (b) EXAFS spectra of Mo/Ce, Cu/Mo/Ce, and Mo/Cu/Ce catalysts, Mo foil, and MoO₃ as references.

scattering, which decrease obviously for the Mo/Ce, Cu/Mo/Ce, Mo/Cu/Ce, implying that Mo is highly dispersed on the CeO₂ surface. Combining the increment of Mo-O bond length from 1.1 Å in MoO₃ reference to 1.3 Å for catalysts and the detection of peak > 955 cm⁻¹ in Raman spectra, we confirm that Mo exists as the octahedral polymeric Mo species rather than single atom or metallic Mo species. The peak around 3 Å in the Cu/Mo/Ce and Mo/Cu/Ce is attributed to the Mo-O-Cu scattering. This peak of the Mo/Cu/Ce shifts to low R value by comparison with the Cu/Mo/Ce, manifesting the shrink of the Mo-O-Cu path due to a stronger interaction between Mo and Cu via the electrons transfer.

The Cu K-edge of the XANES as shown in Fig. 4(a) reveals the coordination environment of Cu. The pre-edge absorption around 8980 eV is assigned to Cu²⁺ dipole-forbidden 1 s→3d transition and peak around 8986 eV is assigned to the 1 s→4p transition of Cu²⁺ with a distorted square-planar or octahedral coordination geometry [37,38]. It can be found that the characteristic peak around 8981 eV in all catalysts is in the Cu₂O and CuO interval, suggesting that the valence state of the copper species is between +1 and +2. Combined with the Cu 2p XPS spectra in Fig. S2(c) and (d), Cu⁺ is the main form in all catalyst and the ratio of Cu⁺/Cu²⁺ follow the sequence of Mo/Cu/Ce > Cu/Mo/Ce > Cu/Ce, which validates the electrons transfer from Mo to Cu. The shift of pre-edge absorption around 8986 eV for the Mo/Cu/Ce towards lower energy testify that more Cu²⁺ are reduced to Cu⁺. EXAFS spectra were performed to investigate the coordination structure and local bond lengths as shown in Figs. 4(b) and S3(b). The strong coordination peak at 1.5 Å is attributed to the first Cu-O coordination with a coordination number of approximately 2.5 for all catalysts, which implies the copper oxides in catalysts is similar to Cu₂O phase. The peaks at 2.1 Å and 2.5 Å are mainly assigned to the Cu-Cu and Cu-O-Ce scatterings [38]. These peaks intensity remarkably decrease for the Cu/Mo/Ce compared to others manifest that less Cu-O-Ce bonds are formed due to part of Cu species are bond to the top of Mo sites. EPR experiments were used to understand the electronic structure of Cu and Mo and the corresponding results were exhibited in Fig. 4(c). After Cu modification, obvious changes are detected for signals below 3450 G. The hyperfine-split signals with spin Hamiltonian parameters of g_{||} = 2.357 with A = 152 G and g_⊥ = 2.058 is associated with Cu²⁺ cations on the surface [37,39]. The intensity around 3336 G in the Cu/Mo/Ce and Mo/Cu/Ce significantly enhances referring to the Cu/Ce. Given that Cu⁺ cations are EPR-silent, this enhancement stems from unpaired electron states of Mo species rather than EPR-active Cu²⁺ species because more Cu²⁺ content is detected in the Cu/Ce, verifying the occurrence of electrons transfer between Mo and Cu. A sharper symmetrical peak intensity in the Mo/Cu/Ce than that in the Cu/Mo/Ce implies a stronger interaction between the Mo and Cu species which is in line with the Mo K-edge XANES. The resonance signal at g = 2.003 is attributed to paramagnetic O₂⁻ species on Ce⁴⁺ cation [40]. This signal intensity enhances for the Mo/Cu/Ce and Cu/Mo/Ce compared with other catalysts, demonstrating that the synergistic effect of Mo and Cu on the transformation of chemisorbed O₂ to O₂⁻ species. Besides, the intensity of Ce⁴⁺-O₂⁻ signal for the Mo/Cu/Ce is stronger than that for the Cu/Mo/Ce. This could be ascribed to the strong electrons transfer from Mo to Cu cation, which triggers the reduction of chemisorbed O₂ on Ce⁴⁺ sites around Cu cation to O₂⁻.

To further study the changes in electronic structure, we calculated total density of states (TDOS) and projected density of states (PDOS) based on the optimized slab models shown in Fig. 2(c-e). The band gap of the Cu/Mo/Ce and Mo/Cu/Ce is apparently narrower than that of the Mo/Ce (Fig. 5), which manifests that electrons are easier to get active and transferred after Cu modification. Meanwhile, Ce f and Mo d orbitals in the conduction band over the Cu/Mo/Ce and Mo/Cu/Ce increase and are closer to the Fermi level by comparison of the Mo/Ce. These results above demonstrate that Cu cations strengthen the conductivity of Mo/Ce system, which is conducive to the activation of low-temperature SCR reaction. The overlapping electron cloud of Ce f and Mo d orbitals in the

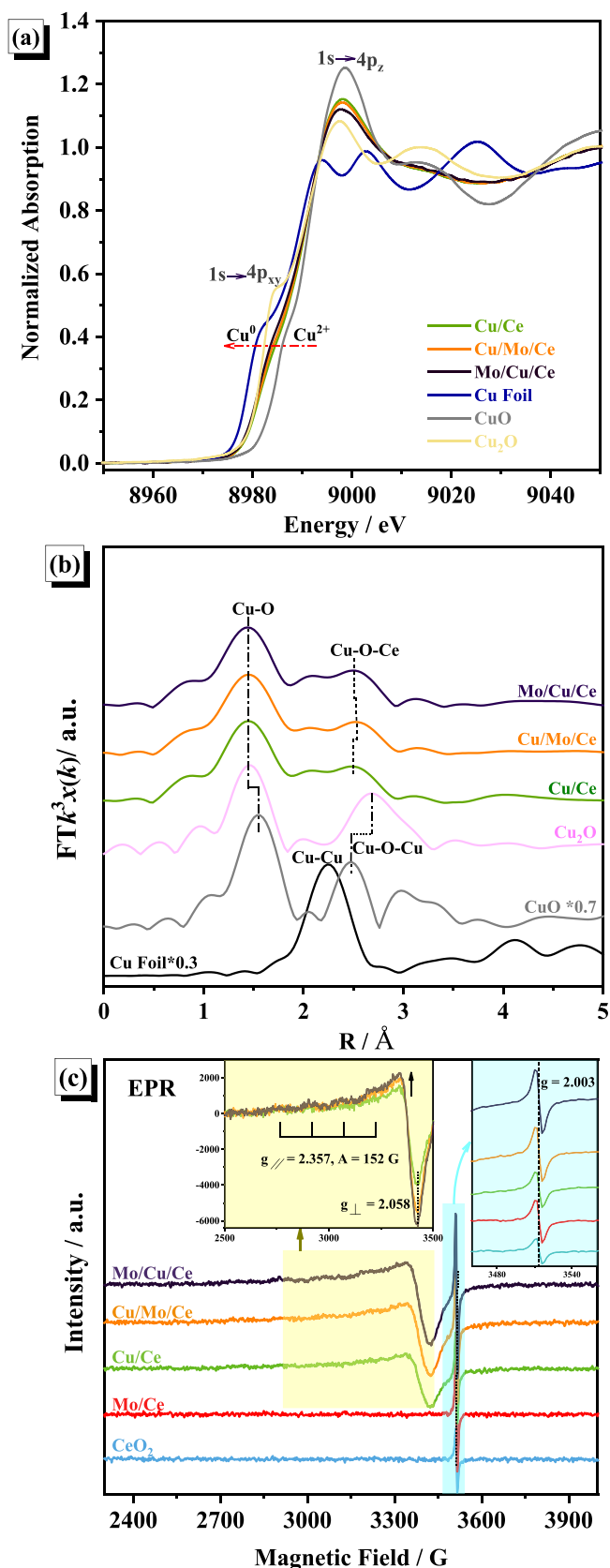


Fig. 4. (a) The normalized Cu K-edge of the XANES and (b) EXAFS spectra of Cu/Ce, Cu/Mo/Ce, Mo/Cu/Ce catalysts, Cu foil, CuO, and Cu₂O as references. (c) EPR spectra of the samples.

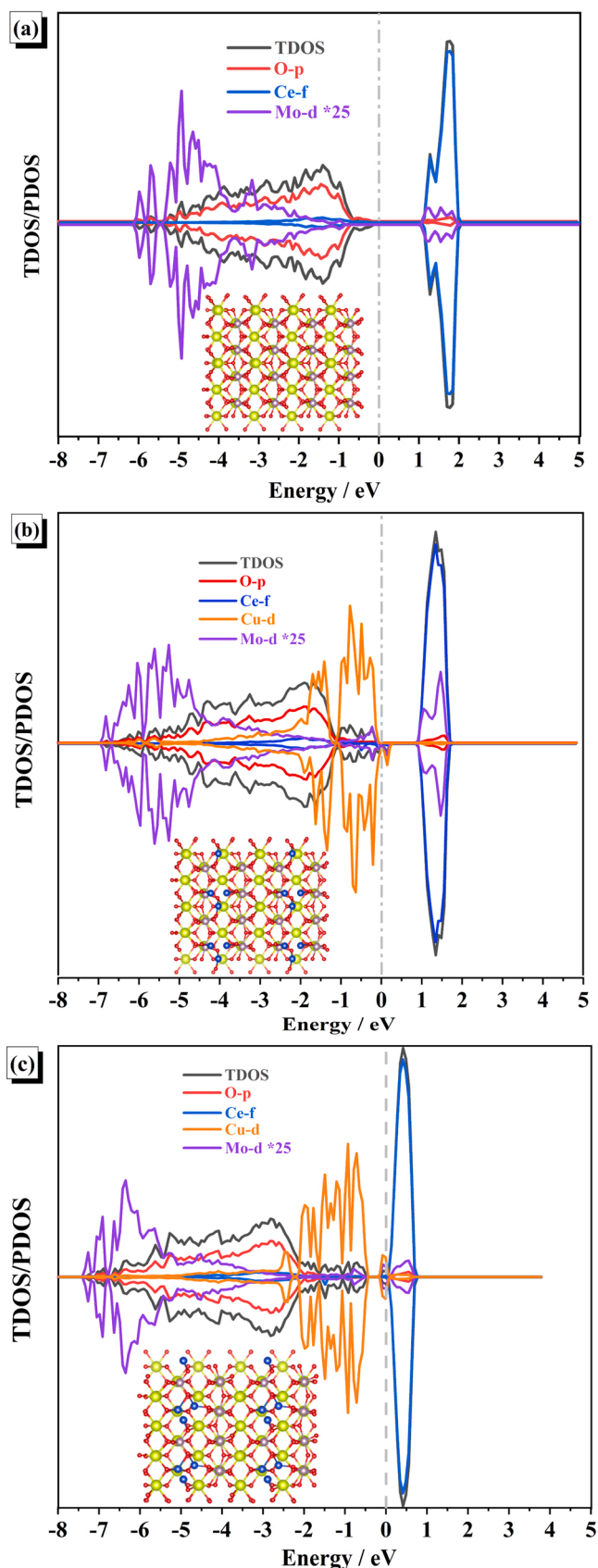


Fig. 5. The TDOS/PDOS of (a) MoO₃/CeO₂ (110), (b) CuO_x/MoO₃/CeO₂ (110), and (c) MoO₃/CuO_x/CeO₂ (110).

conduction band decreases while the overlapping of Cu d and Mo d orbitals increases for the Mo/Cu/Ce in contrast to the Cu/Mo/Ce, which could be attributed to stronger electrons transfer between Mo and Cu via Mo-O-Cu bond. Besides, the decline of Cu d and O p orbitals overlapping in the valence band ranging from -2 to -1 eV could be explained by more Cu⁺ exist in the Mo/Cu/Ce, which is consistent with the results in the Cu K-edge XANES.

H₂-TPR experiments were performed to explore the reducible properties of Cu and Mo oxides over different catalysts (Fig. 6). CeO₂ and Mo/Ce show two similar reduction peaks around 450 and 750 °C, assigned to the reduction of surface and bulk CeO₂ [41]. For Mo/Ce, the peak at 493 °C is attributed to the reduction of Mo-O-Ce species [17]. For Cu/Ce, the peak around 450 °C disappears and a low-temperature reduction peak at 169 °C is detected. This demonstrates that Cu effectively improves the low-temperature reducible properties due to its substitution of Ce in CeO₂ lattice stimulates the generation of oxygen vacancies. Besides, this asymmetric low-temperature peak could also be contributed by the reduction of CuO. The first peak of the Mo/Cu/Ce and Cu/Mo/Ce shifts toward high temperature by comparison with the Cu/Ce and no peaks around 450–493 °C are probed like the reduction peaks of Mo/Ce, verifying again that Mo species are bound around oxygen vacancies and interact with Cu cations by local electron transfer, which results in the moderate reducible performance. Noted that a weak shoulder around 240 °C weakens for the Mo/Cu/Ce relative to the Cu/Mo/Ce, this could be explained by a stronger interaction between Mo and Cu. Concretely, the first loaded Cu could regulate surface electronic structure, further affect the anchor of Mo cations.

To sum up, Cu modification can regulate the surface electronic structure by the substitution of Ce⁴⁺ in the CeO₂ lattice, thereby creates oxygen vacancies as the unsaturated site for the anchor of Mo cations. These Mo cations have polymeric structure with distorted octahedral geometry accompanied by electrons transfer from Mo to Cu, resulting in the moderate reducible properties and the generation of active O₂.

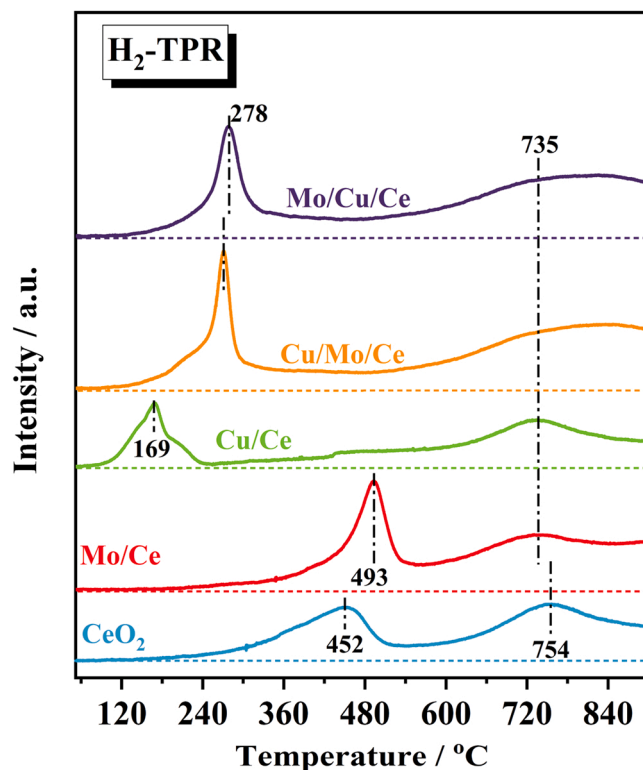


Fig. 6. H₂-TPR curves of CeO₂, Cu/Ce, Mo/Ce, Cu/Mo/Ce, and Mo/Cu/Ce catalysts.

3.3. Effect of copper on the NH₃ and NO adsorption

To investigate the tuning effect of Cu on the SCR reaction for MoO₃/CeO₂ system, we used the TPD experiments and *in situ* DRIFTS to monitor the NH₃ and NO adsorption over the catalysts with increasing temperature. NH₃-TPD profiles and the calculated unit adsorption capacities are exhibited in Fig. 7(a) and Table 1. Generally, three desorption peaks below 200 °C (α), at 200–300 °C (β), and above 300 °C (γ) are correspond to the weak acidity, medium acidity, and strong acidity sites, respectively [42,43]. For the CeO₂ and Cu/Ce, only weak acidity sites are detected and Cu modification causes decline of the NH₃ adsorption capacities from 103.5 to 58.6 mmol·g⁻¹, which caused by the conversion of Ce⁴⁺ to Ce³⁺ by Cu promotion resulting in a weakening of the Lewis acidity. The peaks attributed to medium acidity and strong acidity sites obviously enhance over the Mo/Ce, Cu/Mo/Ce, and Mo/Cu/Ce, suggesting that the exist of Mo could improve the surface acidity of catalyst by providing two types of acid sites, Moⁿ⁺ cation as Lewis acid site and Mo-OH as Brønsted acid site [44]. By comparison with the Mo/Ce, peak β and γ shift to high temperature and the total NH₃ adsorption capacities of the Cu/Mo/Ce and Mo/Cu/Ce drop to 85.5 and 56.7 mmol·g⁻¹, respectively, which are associated with the formation of Mo=O terminals and the local electronic structure change of Mo due to electrons transfer between Mo and Cu according to the XAFS and EPR results. Figs. 7(b), (c), and S4 exhibited the results of *in situ* DRIFTS of catalysts. The characteristic peaks around 1127–1245 and 1615 cm⁻¹ correspond to the coordinated NH₃ adsorbed on Lewis acid sites, and the peaks around 1427 and 1660 cm⁻¹ are attributed to the ion NH₄⁺ bonded to Brønsted acid sites [12,45,46]. The peaks at 1427 and 1659 cm⁻¹ of the Mo/Ce (Fig. 7(b)) are higher than that of the CeO₂ (Fig. S4), which proves the new formation of Brønsted acid sites originated from the Mo-OH structure. However, the corresponding peaks of the Mo/Cu/Ce and Cu/Mo/Ce obviously decrease, suggesting that Cu cations suppress the Mo-OH formation, which could explain the decrease of total NH₃

Table 1

Unit adsorption capacity (mmol·g⁻¹) of NH₃, NO, and NO₂ for CeO₂, Cu/Ce, Mo/Ce, Cu/Mo/Ce, and Mo/Cu/Ce samples obtained from TPD profiles.

	CeO ₂	Cu/Ce	Mo/Ce	Cu/Mo/Ce	Mo/Cu/Ce
NH ₃	103.5	58.6	133.2	85.5	56.7
NO	39.2	53.5	11.8	5.8	5.2
NO ₂	0.1	1.9	0.2	17.1	20.6

adsorption capacities of the Cu/Mo/Ce and Mo/Cu/Ce versus the Mo/Ce. Noted that a new strong peak at 1226 cm⁻¹ is detected on the Mo/Cu/Ce (Fig. 7(c)), this can be ascribed to coordinated NH₃ on a new Lewis acid site derived from Moⁿ⁺ cation in the Mo=O terminals, which could also be found in the spectra of the Cu/Mo/Ce (Fig. S4). The coordinated NH₃ on Moⁿ⁺ cation for the Mo/Cu/Ce and Cu/Mo/Ce shows high stability even at 400 °C that is not probed on the other catalysts. Coordinated NH₃ on Lewis acid site was considered to be more reactive than ion NH₄⁺ on Brønsted acid site and the regeneration of active Lewis acid site was the rate-determining step for the SCR reaction over V₂O₅-WO₃/TiO₂ [18,47]. We speculate that these new Lewis acid sites from Moⁿ⁺ cation also play the same role in the Mo/Cu/Ce. Thus, Cu cations promote the transformation of Mo-OH structure to Mo=O terminals, which acts as a new Lewis acid site. Besides, peak at 1525 cm⁻¹ corresponding to the vibration of NH₂ intermediates remarkably increases on the Cu/Ce (Fig. S4) when the temperature reaches to 225 °C and subsequently consumes at high temperature [48]. This phenomenon could be explained by the dehydrogenation of adsorbed NH₃, indicating high reducible properties of the Cu/Ce can further oxidize NH₂ to NH or N species that react with NO to form N₂O or NO. That is why there is only low NO_x conversion above 225 °C for the Cu/Ce.

NO+O₂-TPD profiles are shown in Fig. 7(d). Generally, low-temperature desorption peaks (< 300 °C) could be assigned to weakly adsorbed NO/NO₂ or nitrites and the high-temperature desorption peaks

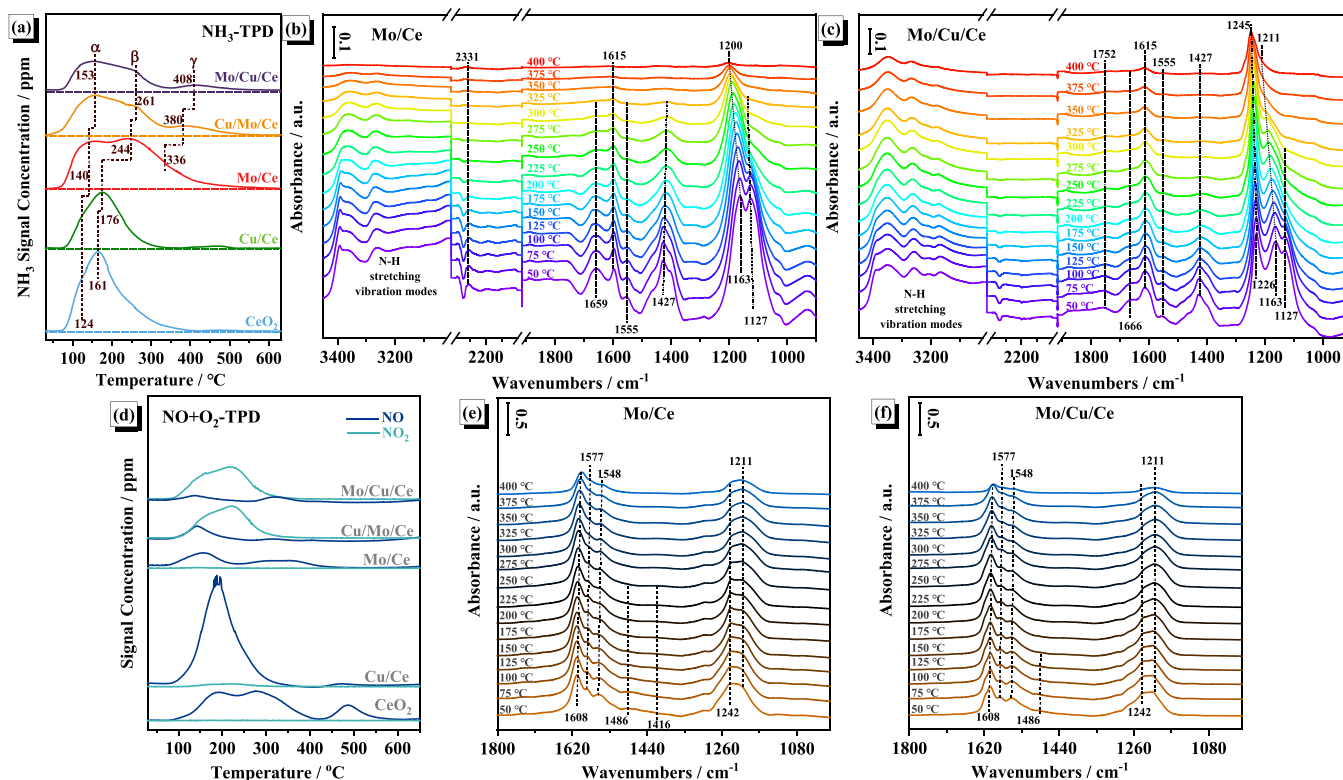
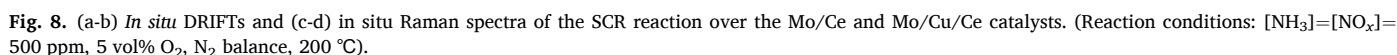


Fig. 7. (a) NH₃-TPD profiles of CeO₂, Cu/Ce, Mo/Ce, Cu/Mo/Ce, and Mo/Cu/Ce samples. *In situ* DRIFTS spectra of NH₃ adsorption-desorption with increasing temperature on the (b) Mo/Ce and (c) Mo/Cu/Ce. (d) NO+O₂-TPD profiles of CeO₂, Cu/Ce, Mo/Ce, Cu/Mo/Ce, and Mo/Cu/Ce. *In situ* DRIFTS spectra of NO+O₂ adsorption-desorption with increasing temperature on the (e) Mo/Ce and (f) Mo/Cu/Ce.

adsorbed NO₂ rather than gaseous NO. That is because the peak at 1242 cm⁻¹ decreased rapidly with increasing temperature, but the NO desorption peaks in TPD experiments were relatively weak. This is also consistent with the rapid disappearance of adsorbed NO₂ peak when the ionic NO₂⁻ is completely consumed above 275 °C. Meanwhile, the peak of nitrates/nitrites on the Mo/Cu/Ce are weaker compared with the Mo/Ce at 400 °C, which manifest that these nitrates/nitrites are unstable on the Mo/Cu/Ce. Based on the above results, it is deduced that NO first adsorbs on the Cu sites to form bridged bidentate NO₂, and then transfer to adjacent Mo sites in the Mo-O-Cu groups which is further oxidized to adsorbed NO₂. We also investigated the NO+O₂ adsorption process on the CeO₂ and Cu/Ce as shown in Fig. S5. A new region at 994–1029 cm⁻¹ assigned to the chelating bidentate NO₃⁻ and monodentate NO₃⁻ is detected for both CeO₂ and Cu/Ce. The peaks corresponding to NO₃⁻ species for CeO₂ are higher than that on other catalysts and they maintain high intensity even at 400 °C. Large amounts of NO₃⁻ species with high thermal stability accumulate on the surface which could combine with the active sites and adsorbed NH₃ species to form ammonium nitrates resulting in the decline of low-temperature SCR activity.

A series of *in situ* DRIFTs and Raman spectra were determined to explore the reactivity of surface adsorbed species during the SCR reaction. Fig. 8(a) and (b) display the consecutive process of NH_3 pre-adsorption, $\text{NO} + \text{O}_2$ adding, NH_3 adding, and $\text{NH}_3 + \text{NO} + \text{O}_2$ adding over the Mo/Ce and Mo/Cu/Ce catalysts at 200 °C. For the Mo/Ce (Fig. 8(a)), all adsorbed NH_3 species (coordinated NH_3 and ion NH_4^+) are consumed quickly. Moreover, the adsorption peaks attributed to NO_2 and NO_3^- are detected when $\text{NO} + \text{O}_2$ adding in the flow, which indicates that all adsorbed NH_3 species are reactive. The following added NH_3 results in the increment of the peak corresponding to adsorbed NH_3 species again. However, peaks at 1240 and 1544 cm^{-1} still maintain the relatively high intensities, and these peaks significantly increase when NH_3 , NO , and O_2 are concomitant in feeding gas, which demonstrates the severe accumulation of ionic NO_2^- and chelating bidentate NO_3^- . These nitrites/nitrates could decompose at the high temperature, but

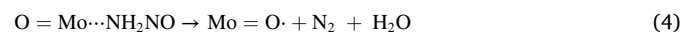
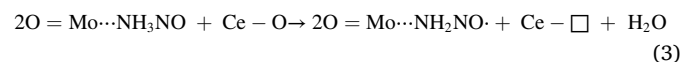
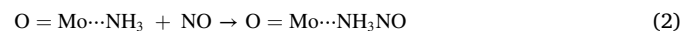


inhibit the conversion of NO at the low temperature. For the Mo/Cu/Ce (Fig. 8(b)), the adsorption peaks of coordinated NH_3 are consumed rapidly in 5 min after $\text{NO} + \text{O}_2$ adding. The peak at 1237 cm^{-1} first increase and then decrease because it is an overlapped peak of ionic NO_2^- and the coordinated NH_3 adsorbed on Lewis acid sites. These ionic NO_2^- can firstly react with adsorbed NH_3 to form ammonium nitrites, then decomposes into N_2 and H_2O . Interestingly, the peak assigned to adsorbed NO_2 cannot be probed in spectra, but two new bands around 1356 and 1439 cm^{-1} , corresponding to monodentate NO_3^- and trans- $\text{N}_2\text{O}_2^{2-}$, respectively, are detected [53]. It is concluded that these adsorbed NO_2 could react with the adsorbed NH_3 to generate new nitrates, afterwards the nitrates are quickly consumed when switching the feeding gas to NH_3 due to the absence of $\text{NO} + \text{O}_2$ replenishing. Besides, the consumption rate of ion NH_4^+ is much lower than that of coordinated NH_3 for the Mo/Cu/Ce, indicating that the Lewis acid site ($\text{Mo}=\text{O}$ bond) take an important role on the SCR reaction, while Brønsted acid site could be a storage site for NH_3 . After the adding of NH_3 , NO , and O_2 in feeding gas, no obvious increment of peaks intensities occurs on the Mo/Cu/Ce, which demonstrates that nitrates can decompose timely to N_2 . Therefore, the SCR reaction on the Mo/Cu/Ce is more efficient than that on the Mo/Ce on account of the new Lewis acid site originated from Mo^{n+} cation in the $\text{Mo}=\text{O}$ terminals as well as the synergistic effect of Cu and Mo in the Mo-O-Cu groups on the formatted high-active nitrates.

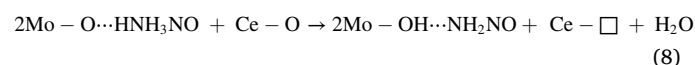
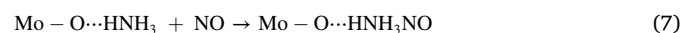
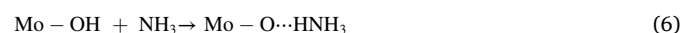
The *in situ* Raman spectra at 200°C of the Mo/Ce and Mo/Cu/Ce are exhibited in the Fig. 8(c) and (d). The peak at 463 cm^{-1} arises from the F_{2g} vibration of CeO_2 increases under the SCR conditions, which is speculated to the redistribution of surface oxygen species. In detail, the changed oxygen species were promoted by the adsorbed SCR reactants on Mo and Cu modified the coordination environment of O in CeO_2 support. The band around 783 cm^{-1} for the Mo/Ce (Fig. 8(c)) shift to high wavenumber under $\text{NO} + \text{O}_2$ atmosphere, indicating that Mo-O-Ce structure provide the sites for the conversion of adsorbed NO to nitrites or nitrates. After introducing the NH_3 in feeding gas, the wavenumber of peak returns to 783 cm^{-1} , indicating the consumption of nitrites/nitrates on the Mo-O-Ce structure. The gradual displacement of this peak to 800 cm^{-1} verifies again that Mo-O-Ce structure creates the NO adsorption sites. The shoulder around 980 cm^{-1} after NH_3 adsorption decreases by comparison with N_2 purge, implying that NH_3 adsorbed on terminal $\text{Mo}=\text{O}$ originated from the octahedral polymeric Mo species which acts as the Lewis acid site [54]. The shoulder of terminal $\text{Mo}=\text{O}$ recovers when introducing $\text{NO} + \text{O}_2$ or $\text{NH}_3 + \text{NO} + \text{O}_2$ in the feeding gas. It is believed that these NH_3 adsorbed species on $\text{Mo}=\text{O}$ are reactive at 200°C . For the Mo/Cu/Ce (Fig. 8(d)), the weak peak around 892 cm^{-1} vanished after NH_3 adsorption. This means that NH_3 adsorbs on the terminal $\text{Mo}=\text{O}$ derived from highly distorted octahedral structure. When adding $\text{NO} + \text{O}_2$ into the feeding gas, the peak around 892 cm^{-1} cannot regain while a new peak around 990 cm^{-1} is detected. Considering that the distorted octahedral structure of Mo oxides results from the Mo-O-Cu bonds, this phenomenon could be explained by the reconstruction of Mo coordination environments driven by SCR reaction, which causes a new terminal $\text{Mo}=\text{O}$ with the low distortion. The peak corresponding to new formed $\text{Mo}=\text{O}$ (990 cm^{-1}) is consumed rapidly during the following NH_3 adsorption process, indicating that this new formed $\text{Mo}=\text{O}$ is a new Lewis acid site, that is in accordance with the *in situ* DRIFTS of NH_3 adsorption results.

The kinetic analysis results verified that the apparent activation energy of Mo/Cu/Ce during the NH_3 -SCR process was 25.1 kJ mol^{-1} lower than that of Mo/Ce catalyst (Fig. 1(c)). And the TOF of the Mo/Cu/Ce is 2.27 times and 2.71 times higher than that of the Mo/Ce at 125°C and 150°C , respectively (Fig. S6). Based on the above results, a mechanism for improving the NH_3 -SCR performance of Mo/Ce catalysts triggered by CuO_x -adding was proposed, in which the following processes occur. For the Mo/Ce, NH_3 firstly adsorbs on the Lewis acid sites provided by the terminal $\text{Mo}=\text{O}$ structure to form the coordinated NH_3 which reacts with NO and surface oxygen to generate NH_2NO , a key intermediate for SCR reaction that can finally decompose into N_2 and

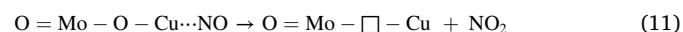
H_2O (Eqs. (1)–(4)). Meanwhile, the reduction of Ce^{4+} to Ce^{3+} occurs in the NH_2NO formation process and Ce^{3+} is oxidized by O_2 to Ce^{4+} , completing a redox cycle (Eq. (5)).



The SCR reaction could also occur at the Mo-OH group as a Brønsted acid site, in which NH_3 adsorbs on the Mo-OH to form ion NH_4^+ (Eq. (6)) and bind with NO to generate NH_4NO intermediates that can further transform to yield N_2 and H_2O after two-step elementary reactions (Eqs. (7)–(9)).

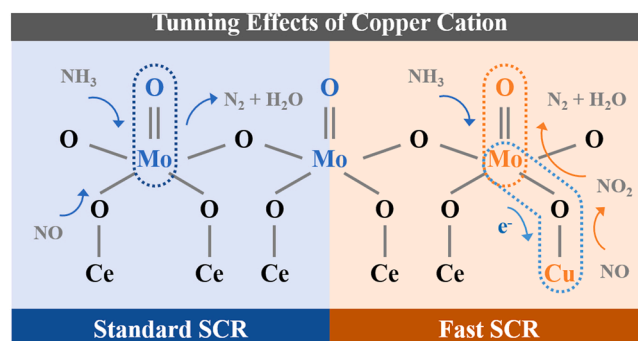


After copper modification (Mo/Cu/Ce), NO can firstly adsorb on the copper sites due to the d orbitals of reduced $\text{Cu}^{\delta+}$ hybridizing with the $2\pi^*$ orbitals of NO (Eq. (10)). Then, the NO group interacts with Mo-O-Cu to form bridged NO_2 finally transforming to adsorbed NO_2 which can react with the coordinated NH_3 and adsorbed NO to produce N_2 and H_2O (Eq. (11)), corresponding to the fast SCR reaction.



The role of copper on SCR reaction is summarized in Scheme 2. Copper ions induce the formation of highly distorted octahedral terminal $\text{Mo}=\text{O}$ groups, and regulates local electronic structure of Mo due to electrons transfer from Mo to Cu, activating the Lewis acid site originated from the $\text{Mo}=\text{O}$. Meanwhile, the Mo-O-Cu pair is conducive to the NO capture and the its further transformation to NO_2 , which is involved in the fast-SCR reaction.

The thermal stability and surface sulfate species content of Mo/Ce and Mo/Cu/Ce catalysts after $\text{SO}_2 + \text{H}_2\text{O}$ tolerance testing were analyzed by TG-FTIR, and the results obtained are displayed in Fig. 9. The weight loss course of two samples can be divided into three steps, wherein step I is caused by the desorption of H_2O on the sample surface, and step II is attributed to the decomposition process of $(\text{NH}_4)_2\text{SO}_4$ and NH_4HSO_4



Scheme 2. Tuning effects of copper cation on the SCR reaction.

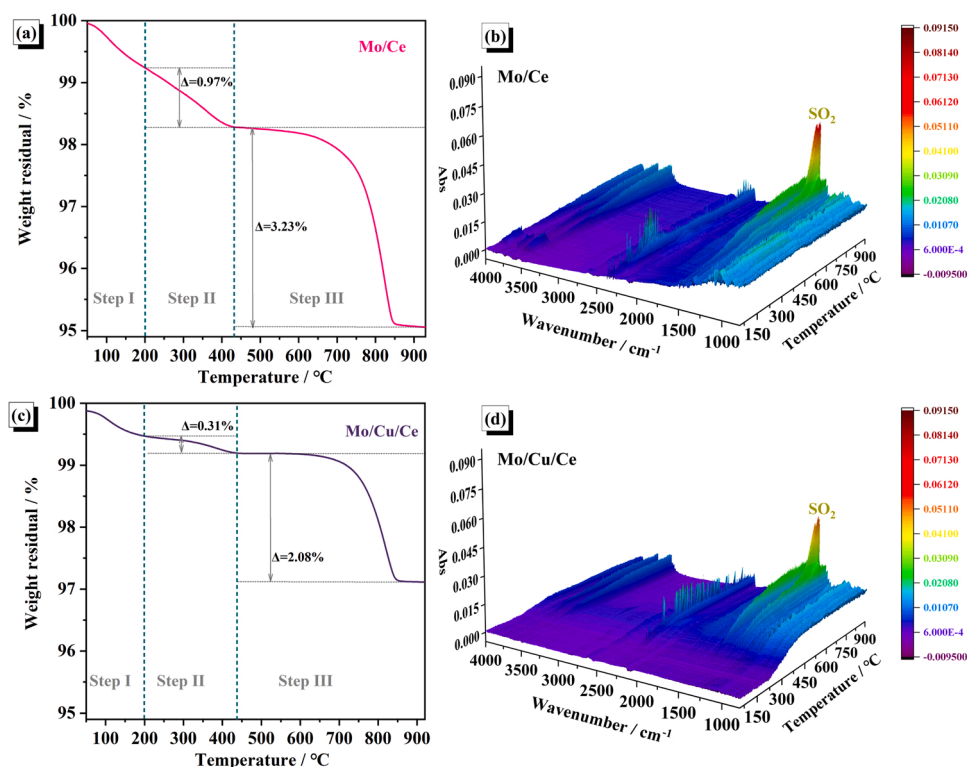


Fig. 9. TG-FTIR results of $\text{SO}_2+\text{H}_2\text{O}$ durability-tested Mo/Ce and Mo/Cu/Ce catalysts. (a, c) TG curve and (b, d) desorption gas FTIR spectra.

deposited on the catalyst surface during the test [51,55]. Compared to 0.97% weight loss of Mo/Ce sample during step II (Fig. 9(a)), it could be seen from Fig. 9(c) that, only 0.31% weight loss of Mo/Cu/Ce was observed, which certifies that $(\text{NH}_4)_2\text{SO}_4$ and NH_4HSO_4 is not inclined to be formed on the surface of Mo/Cu/Ce catalyst. Furthermore, the weight loss process represented by step III is vested in $\text{Ce}(\text{SO}_4)_2$ decomposition [55], which is characterized by the detection of peaks assigned to SO_2 gases at 1390 cm^{-1} through FTIR at this stage (Fig. 9(b) and (d)). Interestingly, Mo/Ce lost 3.23% of its mass during this process, while Mo/Cu/Ce only lost 2.08%. In the meantime, the peak intensity of SO_2 in Mo/Ce catalysts (Fig. 9(b)) is also stronger than that in Mo/Cu/Ce catalysts (Fig. 9(d)). The above results further prove that CuO_x -adding boosts the SO_2 tolerance of Mo/Ce catalysts.

The tuning effect of Cu on the SO_2 resistance was investigated by *in situ* DRIFTS and Raman spectra as shown in Fig. 10. The peaks around 1370 and 1007 cm^{-1} and bands around 1284 , 1135 , and 1097 cm^{-1} belong to the vibration of $\text{S}=\text{O}$ and $\text{S}-\text{O}$ bonds for surface sulfate species [51,56]. The intensities of $\text{S}=\text{O}$ peaks on the Mo/Cu/Ce are weaker than that on the Mo/Ce, indicating that the added Cu can change the bonding mode of sulfate with adsorption sites. Our previous work also found the inhibitory of Cu on the SO_2 adsorption in Cu-doped Mn_3O_4 due to Cu adding, which reducing the amounts of adjacent Mn atoms as the adsorption sites of SO_2 by forming the “-Mn-O-S-O-Mn-” bond [57]. We deduce that Cu plays the same role in the Mo/Ce catalytic system in which Cu prevent the generation of cerium sulfates as shown in the Fig. 9. Fig. 10(b) and (d) shows that *in situ* Raman spectra of the Mo/Ce and Mo/Cu/Ce during SO_2 adsorption. The peak at 463 cm^{-1} on the Mo/Ce remarkably declines but the shoulder around 980 cm^{-1} has only a slight drop, suggesting that SO_2 mainly adsorbs on Ce sites to form cerium sulfates. The decrease of bands around 791 cm^{-1} and the appearance of a new peak around 980 cm^{-1} imply that these sulfates formation alters the interaction between Mo and CeO_2 leading to the transformation of isolated molybdenum to polymeric molybdenum species. For the Mo/Cu/Ce, the peak around 890 cm^{-1} decreases swiftly during SO_2 adsorption. This phenomenon demonstrates that SO_2 prefers

to adsorb on the $\text{Mo}=\text{O}$ terminals with highly distorted octahedral coordinated environments, which protects other active sites and inhibits the generation of cerium sulfates during the SCR reaction. Less sulfates on the Mo/Cu/Ce can provide extra Brønsted acid sites for NH_3 adsorption to form $(\text{NH}_4)_2\text{SO}_4$ and NH_4HSO_4 , which is consistent with the TG-FTIR results where only 0.31% weight loss is observed in the step II.

4. Conclusions

In summary, this case systematically explored the effect of $\text{Cu}^{\delta+}$ species introduction method on the structure-activity relationship of $\text{MoO}_3/\text{CeO}_2$ catalyst. In contrast to the Cu/Ce, Mo/Ce and Cu/Mo/Ce, the Mo/Cu/Ce exhibits the best NH_3 -SCR activity below 300°C and $\text{H}_2\text{O}/\text{SO}_2$ tolerance at 225°C . Further advanced spectroscopy characterizations reveal that the first loaded Cu create unsaturated sites on CeO_2 for Mo anchor inducing the formation of highly distorted octahedral terminal $\text{Mo}=\text{O}$ groups, and regulates local electronic structure of Mo via electrons transfer from Mo to Cu, resulting in the moderate reducible properties and the generation of active O_2^- . Terminal $\text{Mo}=\text{O}$ groups serve as a new Lewis acid site for coordinated NH_3 adsorption and the Mo-O-Cu pair center facilitates the transformation of ionic NO_2^- to NO_2 that is involved in the fast-SCR reaction. Moreover, Cu modification can suppress the yield of $(\text{NH}_4)_2\text{SO}_4$ and NH_4HSO_4 that are harmful to the low-temperature SCR reaction. This active center construction strategy in this work will potentially guide the rational design of efficient low-temperature SCR catalysts and the development at large scale.

CRediT authorship contribution statement

Hao Liu: Conceptualization, Data curation, Formal analysis, Investigation, Methodology, Writing – original draft. **Chuan Gao:** Conceptualization, Formal analysis, Investigation, Methodology. **Jianjun Chen:** Project administration, Funding acquisition, Conceptualization,

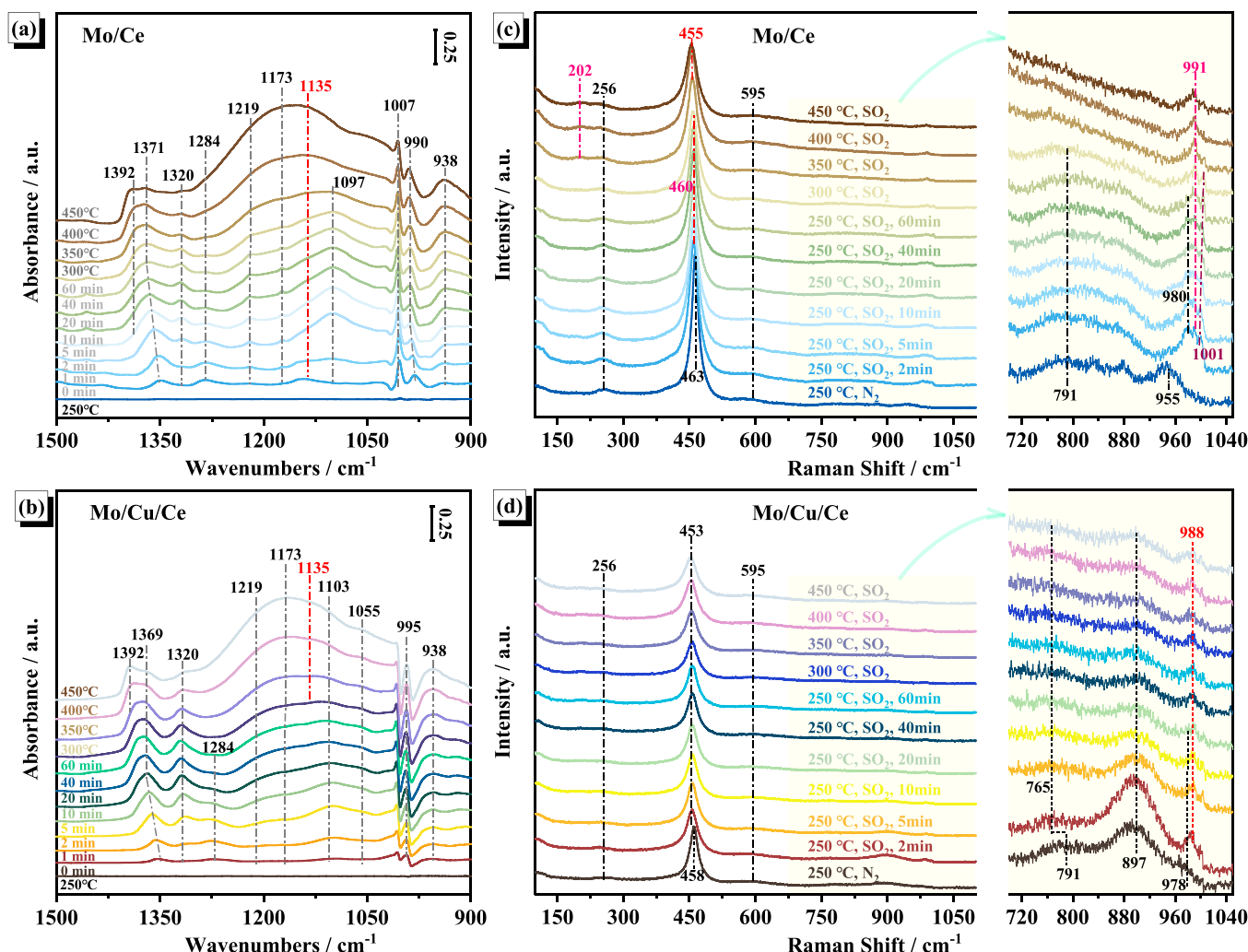


Fig. 10. (a-b) *In situ* DRIFTS and (c-d) *in situ* Raman spectra of SO_2+O_2 co-adsorption over the Mo/Ce and Mo/Cu/Ce catalysts.

Writing – review & editing, Supervision. **Jinxing Mi**: Review, Discussion. **Shan Yang**: Software, Visualization. **Deli Chen**: Investigation, Data curation. **Wenzhe Si**: Supervision. **Yue Peng**: Review, Discussion. **Chuanzhi Sun**: Visualization, Discussion. **Junhua Li**: Project administration, Funding acquisition, Conceptualization, Writing – review & editing, Supervision.

Declaration of Competing Interest

The authors declare that they have no known competing financial interests or personal relationships that could have appeared to influence the work reported in this paper.

Data availability

No data was used for the research described in the article.

Acknowledgments

This work was financially supported by the National Key Research and Development Program of China (2022YFC3701600), and the National Natural Science Foundation of China (22276104, 22022605).

Appendix A. Supplementary material

Supplementary data associated with this article can be found in the

online version at doi:10.1016/j.apcatb.2023.122742.

References

- [1] K. Li, D.J. Jacob, H. Liao, J. Zhu, V. Shah, L. Shen, K.H. Bates, Q. Zhang, S. Zhai, A two-pollutant strategy for improving ozone and particulate air quality in China, *Nat. Geosci.* 12 (2019) 906–910.
- [2] J. Peng, M. Hu, D. Shang, Z. Wu, Z. Du, T. Tan, Y. Wang, F. Zhang, R. Zhang, Explosive secondary aerosol formation during severe haze in the North China Plain, *Environ. Sci. Technol.* 55 (2021) 2189–2207.
- [3] L. Han, S. Cai, M. Gao, J.Y. Hasegawa, P. Wang, J. Zhang, L. Shi, D. Zhang, Selective catalytic reduction of NO_x with NH_3 by using novel catalysts: state of the art and future prospects, *Chem. Rev.* 119 (2019) 10916–10976.
- [4] Z. Lian, J. Wei, W. Shan, Y. Yu, P.M. Radjenovic, H. Zhang, G. He, F. Liu, J.F. Li, Z. Q. Tian, H. He, Adsorption-induced active vanadium species facilitate excellent performance in low-temperature catalytic NO_x abatement, *J. Am. Chem. Soc.* 143 (2021) 10454–10461.
- [5] Y. Inomata, H. Kubota, S. Hata, E. Kiyonaga, K. Morita, K. Yoshida, N. Sakaguchi, T. Toyao, K.I. Shimizu, S. Ishikawa, W. Ueda, M. Haruta, T. Murayama, Bulk tungsten-substituted vanadium oxide for low-temperature NO_x removal in the presence of water, *Nat. Commun.* 12 (2021) 557.
- [6] Z. Hao, Z. Shen, Y. Li, H. Wang, L. Zheng, R. Wang, G. Liu, S. Zhan, The role of alkali metal in $\alpha\text{-MnO}_2$ catalyzed ammonia-selective catalysis, *Angew. Chem. Int. Ed. Engl.* 58 (2019) 6351–6356.
- [7] L.E. Gevers, L.R. Enakonda, A. Shahid, S. Ould-Chikh, C.I.Q. Silva, P.P. Paalanen, A. Aguilar-Tapia, J.L. Hazemann, M.N. Hedhili, F. Wen, J. Ruiz-Martinez, Unraveling the structure and role of Mn and Ce for NO_x reduction in application-relevant catalysts, *Nat. Commun.* 13 (2022) 2960.
- [8] W. Chen, S. Yang, H. Liu, F. Huang, Q. Shao, L. Liu, J. Sun, C. Sun, D. Chen, L. Dong, Single-atom Ce-modified $\alpha\text{-Fe}_2\text{O}_3$ for selective catalytic reduction of NO with NH_3 , *Environ. Sci. Technol.* 56 (2022) 10442–10453.

- [9] W. Qu, X. Liu, J. Chen, Y. Dong, X. Tang, Y. Chen, Single-atom catalysts reveal the dinuclear characteristic of active sites in NO selective reduction with NH_3 , *Nat. Commun.* 11 (2020) 1532.
- [10] X. Fang, W. Qu, T. Qin, X. Hu, L. Chen, Z. Ma, X. Liu, X. Tang, Abatement of nitrogen oxides via selective catalytic reduction over Ce_1W_1 atom-pair sites, *Environ. Sci. Technol.* 56 (2022) 6631–6638.
- [11] Y. Shan, Y. Liu, Y. Li, W. Yang, A review on application of cerium-based oxides in gaseous pollutant purification, *Sep. Purif. Technol.* 250 (2020), 117181.
- [12] S. Xie, W. Tan, Y. Li, L. Ma, S.N. Ehrlich, J. Deng, P. Xu, F. Gao, L. Dong, F. Liu, Copper single atom-triggered niobia–ceria catalyst for efficient low-temperature reduction of nitrogen oxides, *ACS Catal.* 12 (2022) 2441–2453.
- [13] Y. Zhang, S. Zhao, J. Feng, S. Song, W. Shi, D. Wang, H. Zhang, Unraveling the physical chemistry and materials science of CeO_2 -based nanostructures, *Chem* 7 (2021) 2022–2059.
- [14] W. Tan, A. Liu, S. Xie, Y. Yan, T.E. Shaw, Y. Pu, K. Guo, L. Li, S. Yu, F. Gao, F. Liu, L. Dong, Ce-Si mixed oxide: a high sulfur resistant catalyst in the NH_3 -SCR reaction through the mechanism-enhanced process, *Environ. Sci. Technol.* 55 (2021) 4017–4026.
- [15] L. Li, C. Ge, J. Ji, W. Tan, X. Wang, X. Wei, K. Guo, C. Tang, L. Dong, Effects of different methods of introducing Mo on denitration performance and anti- SO_2 poisoning performance of CeO_2 , *Chin. J. Catal.* 42 (2021) 1488–1499.
- [16] S. Xiong, J. Chen, N. Huang, T. Yan, Y. Peng, J. Li, The poisoning mechanism of gaseous HCl on low-temperature SCR catalysts: $\text{MnO}_x\text{--CeO}_2$ as an example, *Appl. Catal. B Environ.* 267 (2020), 118668.
- [17] Y. Peng, R. Qu, X. Zhang, J. Li, The relationship between structure and activity of $\text{MoO}_3\text{--CeO}_2$ catalysts for NO removal: influences of acidity and reducibility, *Chem. Commun.* 49 (2013) 6215–6217.
- [18] M. Zhu, J.K. Lai, U. Tumuluri, Z. Wu, I.E. Wachs, Nature of active sites and surface intermediates during SCR of NO with NH_3 by supported $\text{V}_2\text{O}_5\text{--WO}_3/\text{TiO}_2$ catalysts, *J. Am. Chem. Soc.* 139 (2017) 15624–15627.
- [19] K. Zhu, Q. Zhu, M. Jiang, Y. Zhang, Z. Shao, Z. Geng, X. Wang, H. Zeng, X. Wu, W. Zhang, K. Huang, S. Feng, Modulating $\text{Ti } t_{2g}$ orbital occupancy in a Cu/TiO_2 composite for selective photocatalytic CO_2 reduction to CO, *Angew. Chem. Int. Ed. Engl.* (2022), e202207600.
- [20] L. Li, L. Zhang, K. Ma, W. Zou, Y. Cao, Y. Xiong, C. Tang, L. Dong, Ultra-low loading of copper modified $\text{TiO}_2/\text{CeO}_2$ catalysts for low-temperature selective catalytic reduction of NO by NH_3 , *Appl. Catal. B Environ.* 207 (2017) 366–375.
- [21] K. Murakami, Y. Mizutani, H. Sampei, A. Ishikawa, Y. Tanaka, S. Hayashi, S. Doi, T. Higo, H. Tsuneki, H. Nakai, Y. Sekine, Theoretical prediction by DFT and experimental observation of heterocation-doping effects on hydrogen adsorption and migration over the $\text{CeO}_2(111)$ surface, *Phys. Chem. Chem. Phys.* 23 (2021) 4509–4516.
- [22] B. Liu, J. Liu, L. Xin, T. Zhang, Y. Xu, F. Jiang, X. Liu, Unraveling reactivity descriptors and structure sensitivity in low-temperature NH_3 -SCR reaction over CeTiO_x catalysts: a combined computational and experimental study, *ACS Catal.* 11 (2021) 7613–7636.
- [23] R. Zhou, M. Mohamedali, Y. Ren, Q. Lu, N. Mahinpey, Facile synthesis of multi-layered nanostructured Ni/CeO_2 catalyst plus in-situ pre-treatment for efficient dry reforming of methane, *Appl. Catal. B Environ.* 316 (2022), 121696.
- [24] X. Liu, S. Jia, M. Yang, Y. Tang, Y. Wen, S. Chu, J. Wang, B. Shan, R. Chen, Activation of subnanometric Pt on Cu-modified CeO_2 via redox-coupled atomic layer deposition for CO oxidation, *Nat. Commun.* 11 (2020) 4240.
- [25] Q. Wang, Y. Li, A. Serrano-Lotina, W. Han, R. Portela, R. Wang, M.A. Banares, K. L. Yeung, Operando investigation of toluene oxidation over 1D Pt/CeO_2 derived from Pt cluster-containing MOF, *J. Am. Chem. Soc.* 143 (2021) 196–205.
- [26] A. Li, D. Yao, Y. Yang, W. Yang, Z. Li, J. Lv, S. Huang, Y. Wang, X. Ma, Active $\text{Cu}^0\text{--Cu}^{+}$ sites for the hydrogenation of carbon-oxygen bonds over Cu/CeO_2 catalysts, *ACS Catal.* 12 (2022) 1315–1325.
- [27] Z. Wu, M. Li, J. Howe, H.M. Meyer, S.H. Overbury, Probing defect sites on CeO_2 nanocrystals with well-defined surface planes by Raman spectroscopy and O_2 adsorption, *Langmuir* 26 (2010) 16595–16606.
- [28] R. Radhakrishnan, C. Reed, S.T. Oyama, M. Seman, J.N. Kondo, K. Domen, Y. Ohmami, K. Asakura, Variability in the structure of supported MoO_3 catalysts: studies using raman and x-ray absorption spectroscopy with ab initio calculations, *J. Phys. Chem. B* 105 (2001) 8519–8530.
- [29] J. Zhu, F. Gao, L. Dong, W. Yu, L. Qi, Z. Wang, L. Dong, Y. Chen, Studies on surface structure of $\text{M}_x\text{O}_y/\text{MoO}_3/\text{CeO}_2$ system ($\text{M}=\text{Ni}, \text{Cu}, \text{Fe}$) and its influence on SCR of NO by NH_3 , *Appl. Catal. B Environ.* 95 (2010) 144–152.
- [30] T. Fu, Y. Wang, A. Wernbacher, R. Schlögl, A. Trunschke, Single-site vanadyl species isolated within molybdenum oxide monolayers in propane oxidation, *ACS Catal.* 9 (2019) 4875–4886.
- [31] L. Dong, Y. Chen, The dispersion of molybdena on ceria, *J. Chem. Soc. Faraday Trans.* 92 (1996) 4589–4593.
- [32] J. Zhu, L. Zhang, Y. Deng, B. Liu, L. Dong, F. Gao, K. Sun, L. Dong, Y. Chen, Influence of preparation method on the catalytic activities of $\text{CuO}/\text{Ce}_{0.67}\text{Zr}_{0.33}\text{O}_2$ catalysts in $\text{CO}+\text{O}_2$ reaction, *Appl. Catal. B Environ.* 96 (2010) 449–457.
- [33] Y. Kuwahara, T. Mihogi, K. Hamahara, K. Kusu, H. Kobayashi, H. Yamashita, A quasi-stable molybdenum sub-oxide with abundant oxygen vacancies that promotes CO_2 hydrogenation to methanol, *Chem. Sci.* 12 (2021) 9902–9915.
- [34] L. Wang, X. Duan, X. Liu, J. Gu, R. Si, Y. Qiu, Y. Qiu, D. Shi, F. Chen, X. Sun, J. Lin, J. Sun, Atomically dispersed Mo supported on metallic Co_9S_8 nanoflakes as an advanced noble-metal-free bifunctional water splitting catalyst working in universal pH conditions, *Adv. Energy Mater.* 10 (2019) 1903137.
- [35] Y.N. Zhou, J. Ma, E. Hu, X. Yu, L. Gu, K.W. Nam, L. Chen, Z. Wang, X.Q. Yang, Tuning charge-discharge induced unit cell breathing in layer-structured cathode materials for lithium-ion batteries, *Nat. Commun.* 5 (2014) 5381.
- [36] Z. Yu, H. Yao, Y. Yang, M. Yuan, C. Li, H. He, T.-S. Chan, D. Yan, S. Ma, P. Zapol, M. G. Kanatzidis, $\text{MoO}_x\text{S}_y/\text{Ni}_3\text{S}_2$ microspheres on Ni foam as highly efficient, durable electrocatalysts for hydrogen evolution reaction, *Chem. Mater.* 34 (2022) 798–808.
- [37] L. Kang, B. Wang, Q. Bing, M. Zalibera, R. Buchel, R. Xu, Q. Wang, Y. Liu, D. Gianolio, C.C. Tang, E.K. Gibson, M. Danaie, C. Allen, K. Wu, S. Marlow, L. D. Sun, Q. He, S. Guan, A. Savitsky, J.J. Velasco-Velez, J. Callison, C.W.M. Kay, S. E. Pratsinis, W. Lubitz, J.Y. Liu, F.R. Wang, Adsorption and activation of molecular oxygen over atomic copper(I/II) site on ceria, *Nat. Commun.* 11 (2020) 4008.
- [38] W.Z. Yu, W.W. Wang, S.Q. Li, X.P. Fu, X. Wang, K. Wu, R. Si, C. Ma, C.J. Jia, C. H. Yan, Construction of active site in a sintered copper-ceria nanorod catalyst, *J. Am. Chem. Soc.* 141 (2019) 17548–17557.
- [39] M. Chen, J. Li, W. Xue, S. Wang, J. Han, Y. Wei, D. Mei, Y. Li, J. Yu, Unveiling secondary-ion-promoted catalytic properties of Cu-SSZ-13 zeolites for selective catalytic reduction of NO_x , *J. Am. Chem. Soc.* 144 (2022) 12816–12824.
- [40] S. Keller, U. Bentrup, J. Rabeah, A. Brückner, Impact of dopants on catalysts containing $\text{Ce}_{1-x}\text{M}_x\text{O}_{2.5}$ ($\text{M}=\text{Fe}, \text{Sb}$ or Bi) in NH_3 -SCR of NO_x —a multiple spectroscopic approach, *J. Catal.* 408 (2022) 453–464.
- [41] Z. Su, W. Si, H. Liu, S. Xiong, X. Chu, W. Yang, Y. Peng, J. Chen, X. Cao, J. Li, Boosting the catalytic performance of CeO_2 in toluene combustion via the Ce-Ce homogeneous interface, *Environ. Sci. Technol.* 55 (2021) 12630–12639.
- [42] L. Kang, L. Han, P. Wang, C. Feng, J. Zhang, T. Yan, J. Deng, L. Shi, D. Zhang, SO_2 -tolerant NO_x reduction by marvelously suppressing SO_2 adsorption over $\text{Fe}_3\text{Ce}_{1-x}\text{VO}_4$ catalysts, *Environ. Sci. Technol.* 54 (2020) 14066–14075.
- [43] X. Qi, L. Han, J. Deng, T. Lan, F. Wang, L. Shi, D. Zhang, SO_2 -tolerant catalytic reduction of NO_x via tailoring electron transfer between surface iron sulfate and subsurface ceria, *Environ. Sci. Technol.* 56 (2022) 5840–5848.
- [44] H. Chang, M.T. Jong, C. Wang, R. Qu, Y. Du, J. Li, J. Hao, Design strategies for P-containing fuels adaptable $\text{CeO}_2\text{--MoO}_3$ catalysts for DeNO_x : significance of phosphorus resistance and N_2 selectivity, *Environ. Sci. Technol.* 47 (2013) 11692–11699.
- [45] M.N. Khan, L. Han, P. Wang, D. Zhang, Tailored alkali resistance of DeNO_x catalysts by improving redox properties and activating adsorbed reactive species, *iScience* 23 (2020), 101173.
- [46] Z. Zhang, R. Li, M. Wang, Y. Li, Y. Tong, P. Yang, Y. Zhu, Two steps synthesis of CeTiO_x oxides nanotube catalyst: Enhanced activity, resistance of SO_2 and H_2O for low temperature NH_3 -SCR of NO_x , *Appl. Catal. B Environ.* 282 (2021), 119542.
- [47] A. Marberger, D. Ferri, M. Elsener, O. Krocher, The significance of lewis acid sites for the selective catalytic reduction of nitric oxide on vanadium-based catalysts, *Angew. Chem. Int. Ed. Engl.* 55 (2016) 11989–11994.
- [48] X. Yao, L. Zhang, L. Li, L. Liu, Y. Cao, X. Dong, F. Gao, Y. Deng, C. Tang, Z. Chen, L. Dong, Y. Chen, Investigation of the structure, acidity, and catalytic performance of $\text{CuO}/\text{Ti}_{0.95}\text{Ce}_{0.05}\text{O}_2$ catalyst for the selective catalytic reduction of NO by NH_3 at low temperature, *Appl. Catal. B Environ.* 150–151 (2014) 315–329.
- [49] H. Hu, S. Cai, H. Li, L. Huang, L. Shi, D. Zhang, Mechanistic aspects of deNO_x processing over TiO_2 supported Co–Mn oxide catalysts: structure–activity relationships and *in situ* DRIFTS analysis, *ACS Catal.* 5 (2015) 6069–6077.
- [50] Y. Peng, D. Wang, B. Li, C. Wang, J. Li, J. Crittenden, J. Hao, Impacts of Pb and SO_2 Poisoning on $\text{CeO}_2\text{--WO}_3/\text{TiO}_2\text{--SiO}_2$ SCR Catalyst, *Environ. Sci. Technol.* 51 (2017) 11943–11949.
- [51] H. Liu, Z. Fan, C. Sun, S. Yu, S. Feng, W. Chen, D. Chen, C. Tang, F. Gao, L. Dong, Improved activity and significant SO_2 tolerance of samarium modified $\text{CeO}_2\text{--TiO}_2$ catalyst for NO selective catalytic reduction with NH_3 , *Appl. Catal. B Environ.* 244 (2019) 671–683.
- [52] J. Liu, X. Li, Q. Zhao, J. Ke, H. Xiao, X. Lv, S. Liu, M. Tadé, S. Wang, Mechanistic investigation of the enhanced NH_3 -SCR on cobalt-decorated Ce–Ti mixed oxide: In situ FTIR analysis for structure–activity correlation, *Appl. Catal. B Environ.* 200 (2017) 297–308.
- [53] G. Qi, R.T. Yang, R. Chang, $\text{MnO}_x\text{--CeO}_2$ mixed oxides prepared by co-precipitation for selective catalytic reduction of NO with NH_3 at low temperatures, *Appl. Catal. B Environ.* 51 (2004) 93–106.
- [54] X. Li, J. Li, Y. Peng, X. Li, K. Li, J. Hao, Comparison of the structures and mechanism of arsenic deactivation of $\text{CeO}_2\text{--MoO}_3$ and $\text{CeO}_2\text{--WO}_3$ SCR catalysts, *J. Phys. Chem. C* 120 (2016) 18005–18014.
- [55] K. Guo, J. Ji, W. Song, J. Sun, C. Tang, L. Dong, Conquering ammonium bisulfate poison over low-temperature NH_3 -SCR catalysts: a critical review, *Appl. Catal. B Environ.* 297 (2021), 120388.
- [56] H. Liu, C. Sun, Z. Fan, X. Jia, J. Sun, F. Gao, C. Tang, L. Dong, Doping effect of Sm on the $\text{TiO}_2/\text{CeSmO}_x$ catalyst in the NH_3 -SCR reaction: structure–activity relationship, reaction mechanism and SO_2 tolerance, *Catal. Sci. Technol.* 9 (2019) 3554–3567.
- [57] S. Xiong, Y. Peng, D. Wang, N. Huang, Q. Zhang, S. Yang, J. Chen, J. Li, The role of the Cu dopant on a Mn_3O_4 spinel SCR catalyst: improvement of low-temperature activity and sulfur resistance, *Chem. Eng. J.* 387 (2020), 124090.